nature chemistry

Article https://doi.org/10.1038/s41557-022-01064-2

A soil-inspired dynamically responsive chemical system for microbial modulation

In the format provided by the authors and unedited

Supplementary Materials for

A Soil-Inspired Dynamically Responsive Chemical System for Microbial Modulation

Yiliang Lin[1]†*, Xiang Gao[1]†, Jiping Yue[2]†, Yin Fang[1]†, Jiuyun Shi[2], Lingyuan Meng[3], Clementene Clayton[2], Xin-Xing Zhang[1,2,4], Fengyuan Shi[5], Junjing Deng[6], Si Chen[6], Yi Jiang[6], Fabricio Marin[6], Jingtian Hu[7], Hsiu-Ming Tsai[8], Qing Tu[9], Eric W. Roth[10], Reiner Bleher[9,10], Xinqi Chen[10], Philip Griffin[4], Zhonghou Cai[6], Aleksander Prominski[1,2,4], Teri W. Odom[7,9], Bozhi Tian[1,2,3]*

[1]The James Franck Institute, University of Chicago, Chicago, IL 60637, USA

[2]Department of Chemistry, University of Chicago, Chicago, IL 60637, USA

[3]Pritzker School of Molecular Engineering, University of Chicago, Chicago, IL 60637, USA

[4]The Institute for Biophysical Dynamics, University of Chicago, Chicago, IL 60637, USA

[5]Electron Microscopy Core, Research Resources Center, University of Illinois Chicago, Chicago, IL 60607, USA

[6]Advanced Photon Source, Argonne National Laboratory, Lemont, IL 60439, USA

[7]Department of Chemistry, Northwestern University, Evanston, IL 60208, USA

[8]Department of Radiology, University of Chicago, Chicago, IL 60637, USA

[9]Department of Materials Science and Engineering, Northwestern University, Evanston, IL 60208, USA

[10]NUANCE Center, Northwestern University, Evanston, IL 60208, USA

†These authors contributed equally to this work.

*Correspondence to: btian@uchicago.edu, yilianglin@uchicago.edu

This PDF file includes:

- Materials and Methods
- Supplementary Tables 1 and 2
- Supplementary Figures 1 to 51
- Caption for Supplementary Video 1

Other Supplementary Materials for this manuscript include the following:

Supplementary Video 1

Materials and Methods

Supplementary Table 1. Roles of the individual components in the soil-inspired chemical system.

Roles	Components			Figure panels
	Liquid metal	*Starch granules*	*Nanoclay particles*	
Mechanical		Establish the porosity	Establish the porosity	Figs, 1e, 1f, 2e
Mechanical	Establish a macroscopic shape	Establish a macroscopic shape	Establish a macroscopic shape	Fig. S5
Mechanical		Organic glue to maintain the soil-inspired material		Figs. 2f, S11-S14
Mechanical			Tune the modulus	Figs. 3a, S16
Mechanical	Increase the modulus and toughness of the composite			Fig. S17
Mechanical		Enable local deformability (through the porosity)	Enable local deformability (through the porosity)	Fig. 3b, S18
Physical and chemical	Enable mechanically-induced electrical conductivity increase	Facilitate liquid metal spreading during the indentation (through the porosity)	Facilitate liquid metal spreading during the indentation (through the porosity)	Figs. 3b, 3c
Physical and chemical	Enable chemically-induced electrical conductivity decrease	Permit vapor diffusion (through the porosity)	Permit vapor diffusion (through the porosity)	Fig. 3d,3e
Physical and chemical	Enable optically-induced electrical conductivity increase (through liquid metal redistribution)			Figs. 4a
Physical and chemical		Enable optically-induced electrical conductivity increase (through carbonization)		Figs. 4e, 4f
Biological	Enhance microbial biofilm growth and liquid culture	Enhance microbial biofilm growth and liquid culture	Enhance microbial biofilm growth and liquid culture	Figs. 4g, S31, S32a
Biological	Enhance the biofuel production	Enhance the biofuel production	Enhance the biofuel production	Fig. S32b
Biological	Enrich bacterial diversity under the tetracycline-induced dysbiosis *in vivo*	Enrich bacterial diversity under the tetracycline-induced dysbiosis *in vivo*	Enrich bacterial diversity under the tetracycline-induced dysbiosis *in vivo*	Figs. 5a, S42
Biological	Contribute to the alleviation of some DSS-induced colitis symptoms, including body weight loss, colon length shortening, fecal blooding score, but not on fecal water content or histology injury score of the colon.	Contribute to the alleviation of some DSS-induced colitis symptoms, including body weight loss, colon length shortening, fecal blooding score, and fecal water content, but not on histology injury score of the colon.		Figs. 5f-5k

	Rectify colonic *Romboustsia* dysbiosis *in vivo*			Figs. S48

Supplementary Table 2. Band Assignments for the Infrared Spectra.

Species	Frequency (cm^{-1})	Assignment
H_2O	1640	bending[9]
	2105	bending+libration[9]
	3350	OH stretching[9]
D_2O	1207	bending[9,10]
	1560	bending+libration[9,10]
	2455	OD stretching[9]
HDO	1458	bending[10]
Starch	966	skeletal mode vibrations of α-1,4 glycosidic linkage[11,12]
	1007	C-O-H deformation[13,14]
	1087	C-O, C-C stretching[15]
	1168	asymmetric stretching of C-O-C glycosidic bridge[14]
	1307	C-H deformation of all ring hydrogens[15]
	1332	C-O-H bending + CH_2 twisting[15]
	1371&1386	ring mode[15]
	2884&2930	C-H deformation[15]

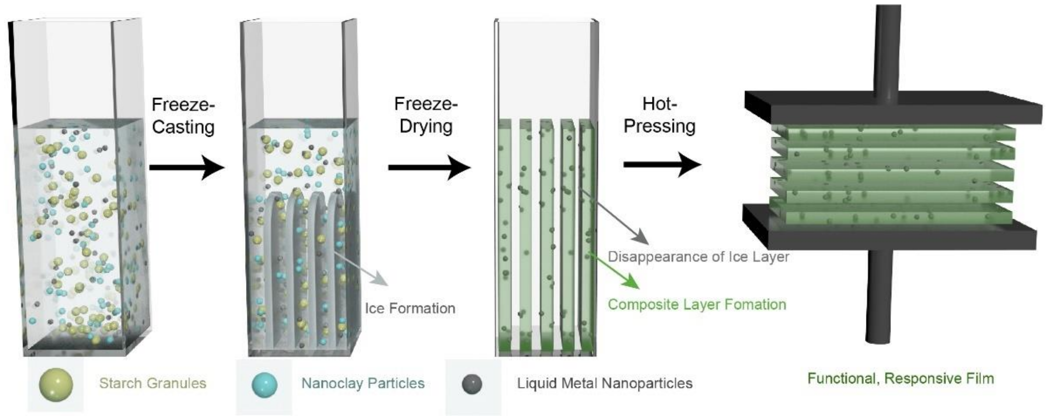

Supplementary Fig. 1 | Schematic of the fabrication of the soil-inspired chemical system. Here we use a rectangular container as an example. The choice of the container determines the shape and scale of the soil-inspired material. The fabrication procedure includes freeze-casting, freeze-drying, and hot-pressing processes.

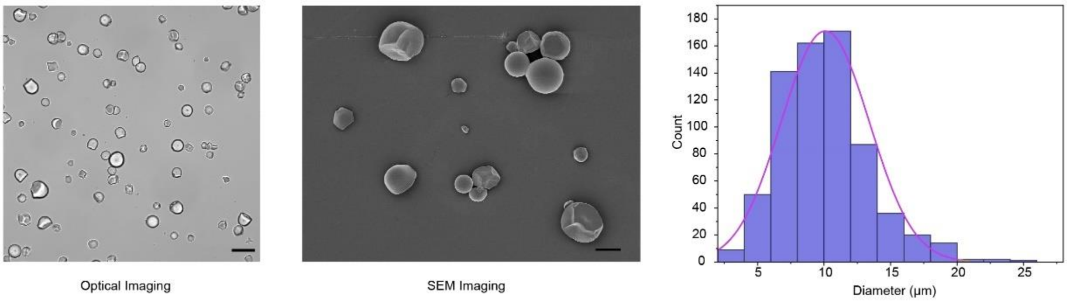

Supplementary Fig. 2 | The starch granules have an average lateral size of ~ 10.1 μm. The figure shows the optical and SEM images of starch granules and the corresponding size distribution for ~700 random particles. Scale bar, 30 μm (left), and 10 μm (middle).

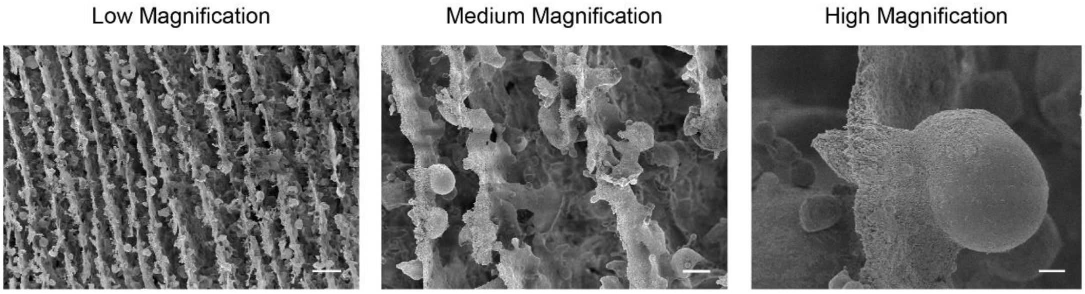

Supplementary Fig. 3 | Freeze-drying yields layered structure with liquid metal particles and starch granules attached on the layer surfaces. SEM images show the porous scaffold morphology at different magnifications. The sample was recorded prior to the hot-pressing step. From left to right, scale bars are 40 μm, 10 μm, and 2 μm.

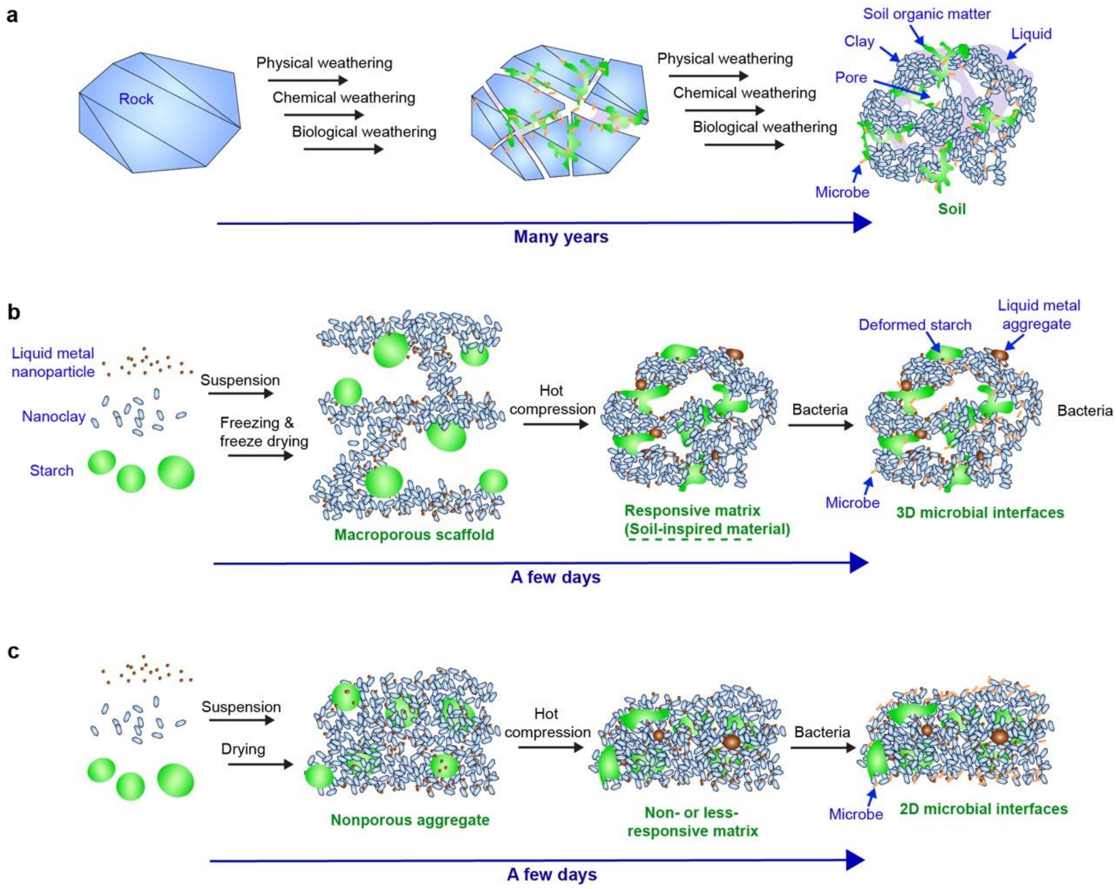

Supplementary Fig. 4 | Freeze-drying is a scalable method for soil-inspired material preparation. a) Schematic showing the formation of the porous soil structure due to years of physical, chemical, and biological weathering. b) Schematic showing our approach, using the freeze-drying method to build a microporous scaffold followed by hot compression to form 3D microbial interfaces. The liquid-metal and starch granules attach mainly to the surface of the mineral-based layers, which is critical for the responsive properties and microbial modulation activities. c) Schematic showing how simple mixing in suspension would produce a nonporous aggregate, which only yields 2D microbial interfaces. The nonporous composite does not show any of the responsive properties revealed in this study (**Fig. 3**).

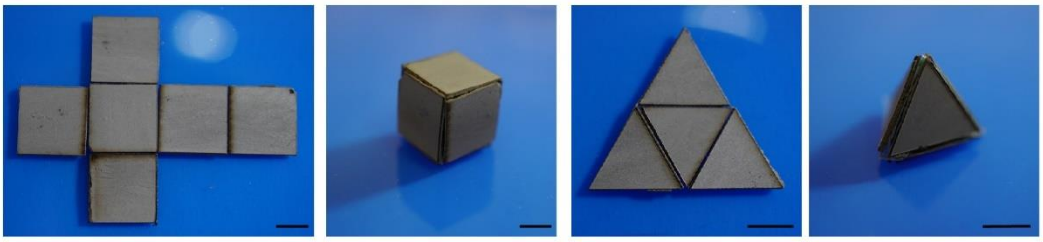

Supplementary Fig. 5 | Photographs of the soil-inspired material fabricated into origami structures. The composite materials can be prepared into different building blocks, and can be assembled into origami structures with polymer joints. Scale bar, 5 mm.

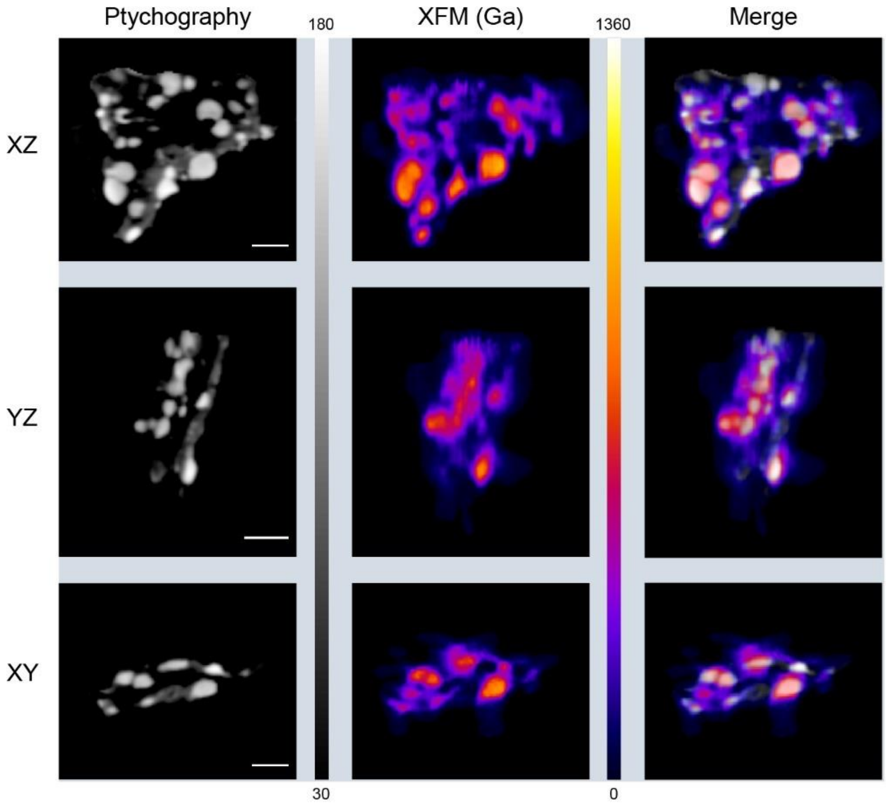

Supplementary Fig. 6 | Sectioning of correlative 3D x-ray fluorescence and ptychographic tomography at different planes confirms the distribution of gallium-based liquid metal particles. The electron-dense particles in ptychography correlate with the gallium distribution in x-ray fluorescence imaging, confirming that the bright particles in ptychography are gallium-based liquid metal particles. Scale bar, 2 μm.

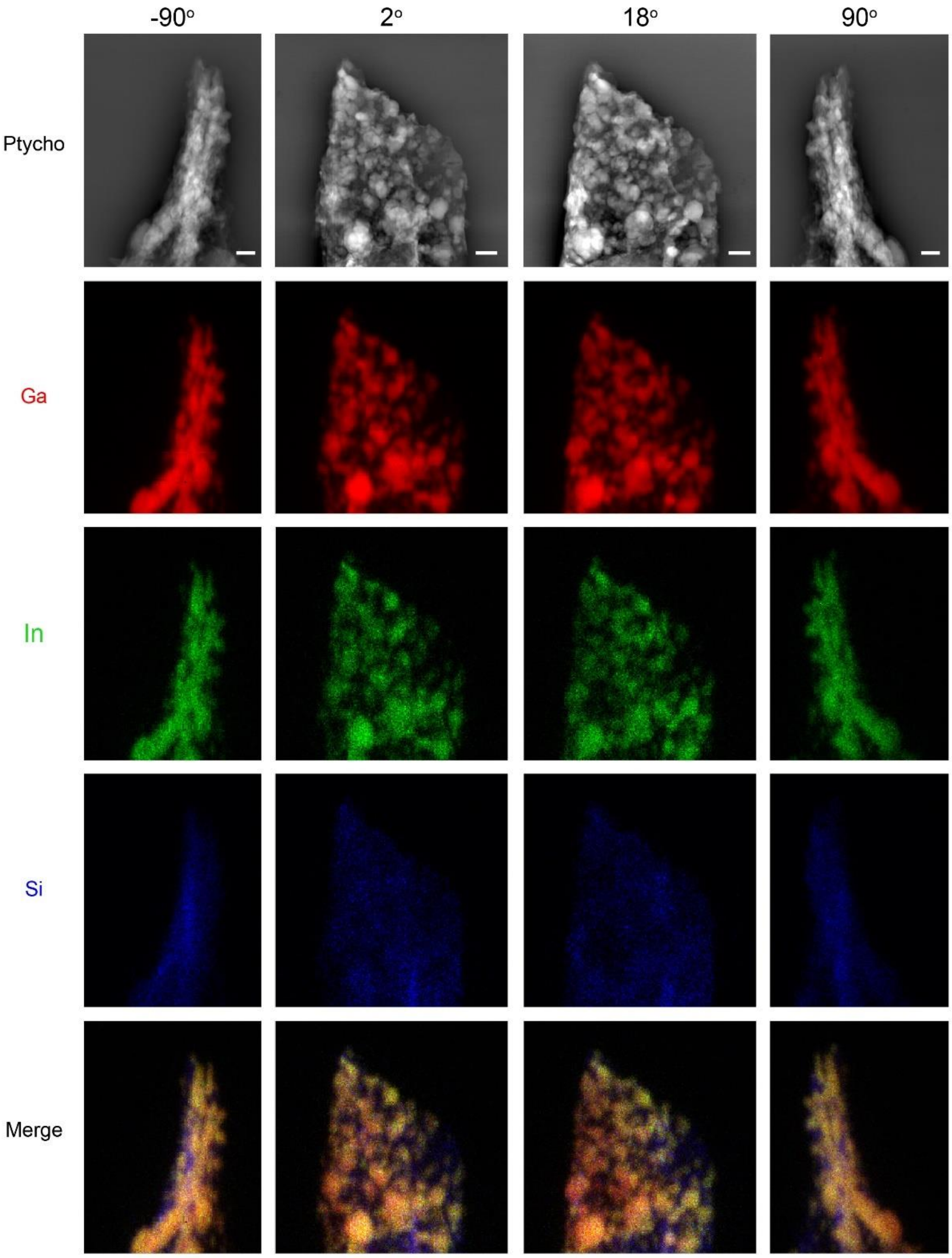

Supplementary Fig. 7 | X-ray ptychography and fluorescence imaging confirm the distribution of liquid metal and nanoclay in the soil-inspired material. 3D x-ray ptychography and fluorescence imaging were collected at different projections (-90°/2°/18°/90°) on soil-inspired material. X-ray fluorescence element mappings show the distribution of Ga (red) and In (green) from liquid metal, and Si(blue) from nanoclay. Scale bar, 2 μm.

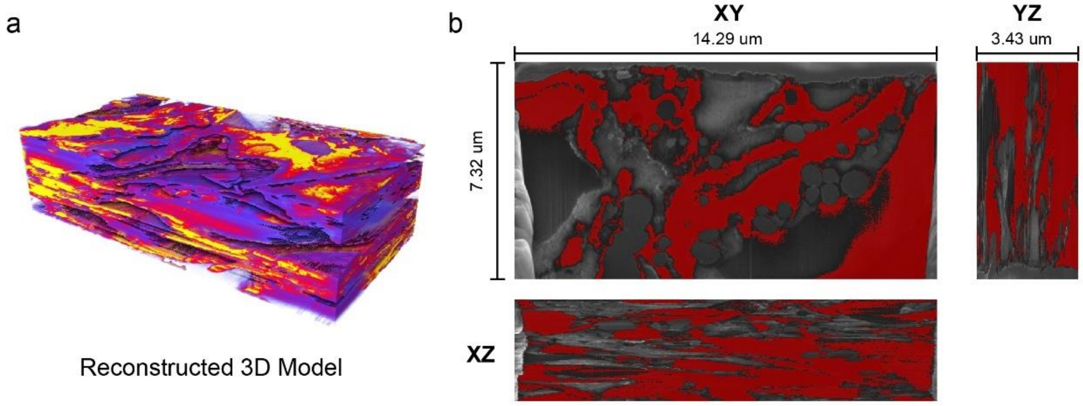

Supplementary Fig. 8 | 3D reconstruction of FIB confirms the porosity of soil-inspired material. a) A reconstructed 3D model. b) Representative slices in the 3D model with porous domains highlighted in red. Calculation from the whole sample yields a porosity of ~54.6%.

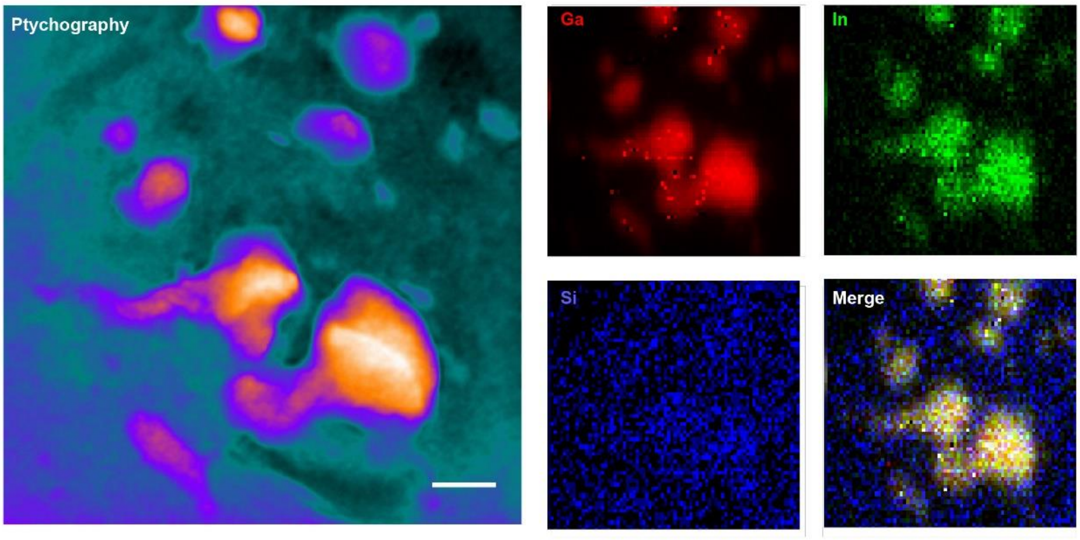

Supplementary Fig. 9 | X-ray ptychography and fluorescence imaging in cross-sectioned samples confirm the distribution of elements. Electron density in the ptychography is shown using a color scale. X-ray fluorescence element mapping (right) shows the distribution of Ga (red) and In (green) from liquid metal, and Si (blue) from nanoclay. Scale bar, 500 nm.

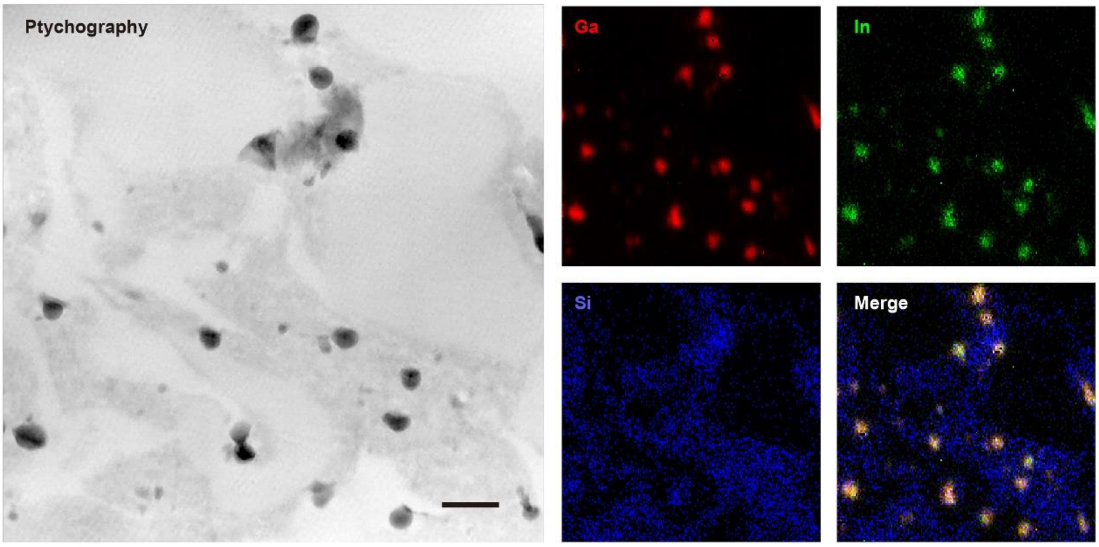

Supplementary Fig. 10 | X-ray ptychography and fluorescence imaging in cross-sectioned samples confirm the distribution of elements. Electron density in the ptychography is shown in greyscale. X-ray fluorescence element mapping (right) shows the distribution of Ga (red) and In (green) from liquid metal, and Si (blue) from nanoclay. Scale bar, 1 µm.

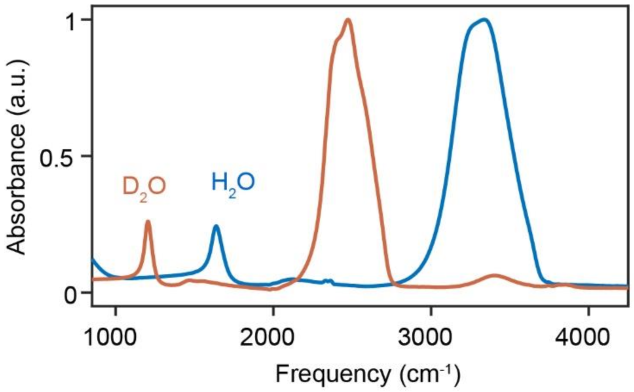

Supplementary Fig. 11 | Fourier-transform infrared (FTIR) spectra of water and heavy water in the frequency range 880 to 4250 cm^{-1}.

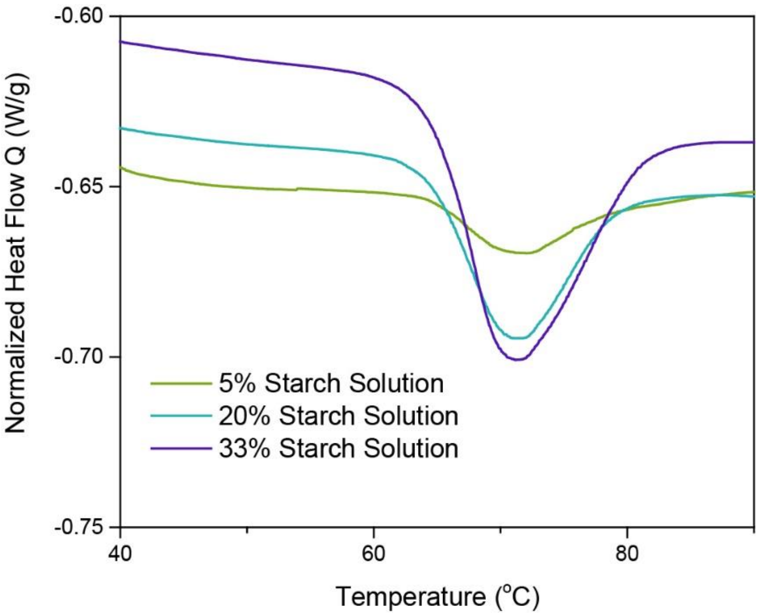

Supplementary Fig. 12 | Differential scanning calorimetry (DSC) curves indicate a phase change temperature of ~70 ºC. The phase transition correlates with loss of crystallinity as the starch gelatinization process progresses.

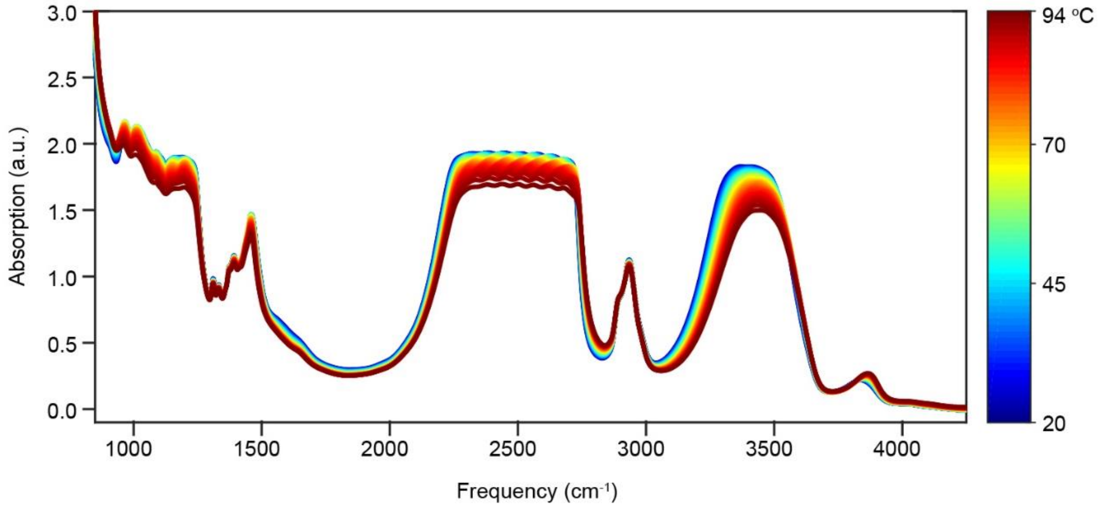

Supplementary Fig. 13 | The gelatinization process is not reversible. Temperature ramp FTIR spectra of starch from 94 ºC to 20 ºC show minimal changes with decreasing temperature, in contrast with the heating spectra, indicating that the chemical changes during the gelatinization process are irreversible.

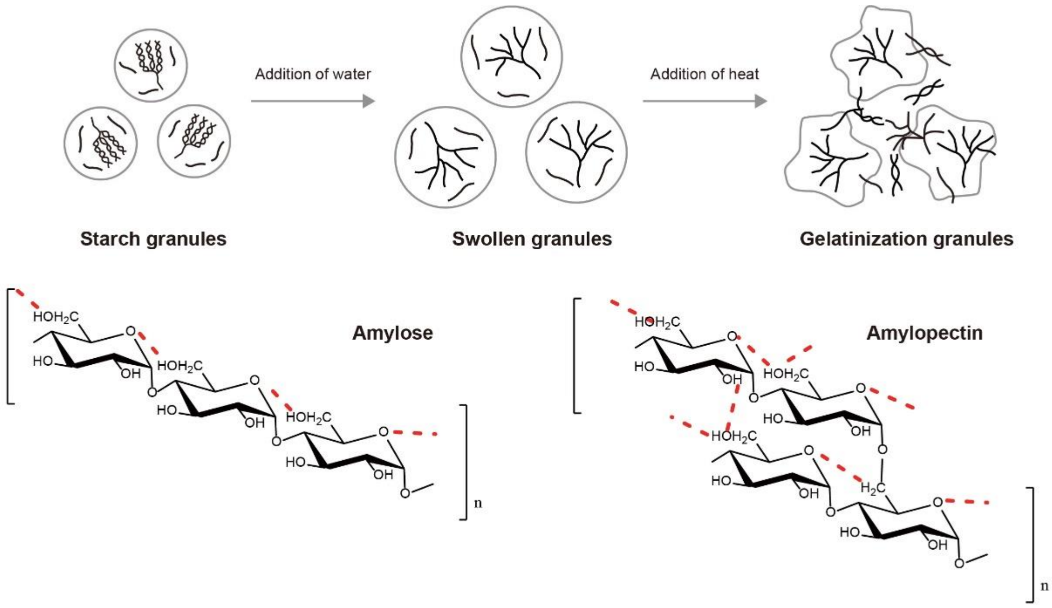

Supplementary Fig. 14 | Schematic diagrams show the starch gelatinization and the chemical structures of starch. During gelatinization, the addition of water breaks the amylose crystallinity and disrupts helices. More heat and water then cause more swelling and amylose diffusion out of the granules. As a result, the water outside the starch diffuses in and forms intermolecular hydrogen bonds. The red dash lines in the chemical structure represent hydrogen bonds.

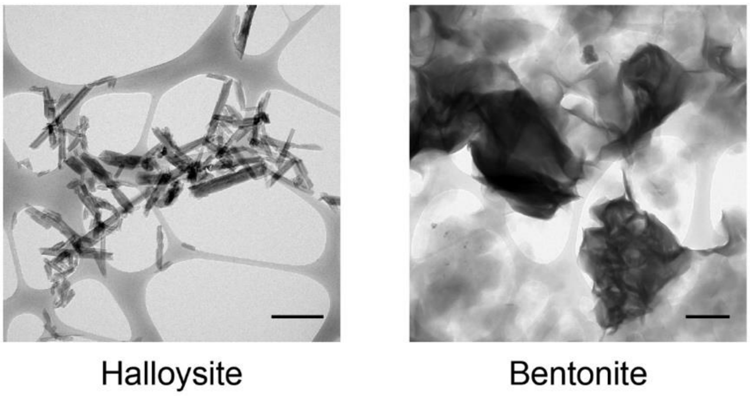

Supplementary Fig. 15 | Different nanoclays can be used to construct the soil-inspired chemical systems. In this paper, we highlighted two nanoclays, halloysite and bentonite nanoclay, which have very different morphologies. Scale bar, 500 nm.

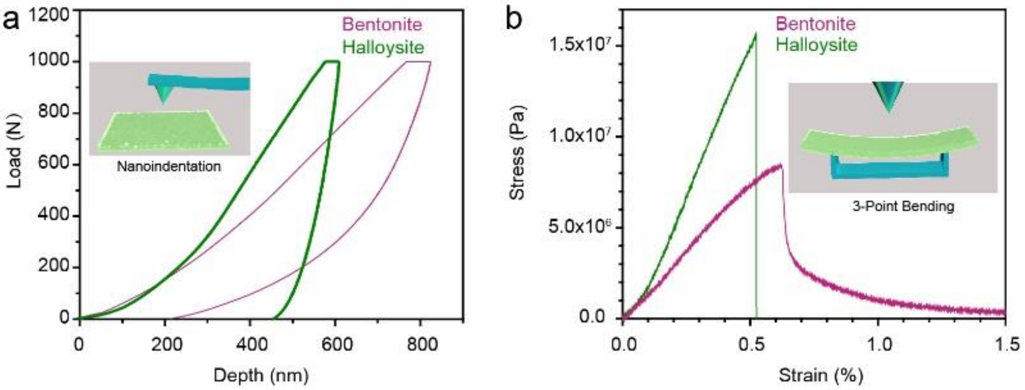

Supplementary Fig. 16 | The Young's moduli of soil-inspired material can range from 2 to 5 GPa through choices of nanoclays and their ratios in the composites. a) A schematic and typical curves of the soil-inspired material under nanoindentation. Nanoindentation is a microscopic test that probes the sample surface in a local area. b) A schematic and typical curves of soil-inspired material under three-point bending. Three-point bending in the dynamic mechanical analyzer is a standard technique to measure the bulk mechanical properties of a material.

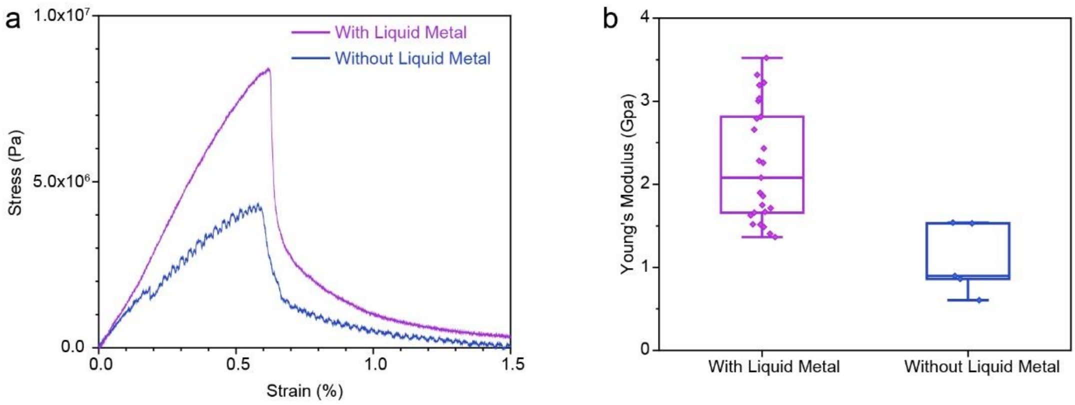

Supplementary Fig. 17 | The mechanical properties of soil-inspired materials are influenced by liquid metal. a) Typical strain-stress curves from three-point-bending tests of soil-inspired materials, with and without liquid metal. b) Statistical analysis shows the soil-inspired material without liquid metal possesses a Young's modulus ~ half that of complete composite. Box bind interquartile range (IQR) divided by the median; whiskers extend 1.5 ± IQR. n = 25 for sample with liquid metal and n = 5 for sample without liquid metal.

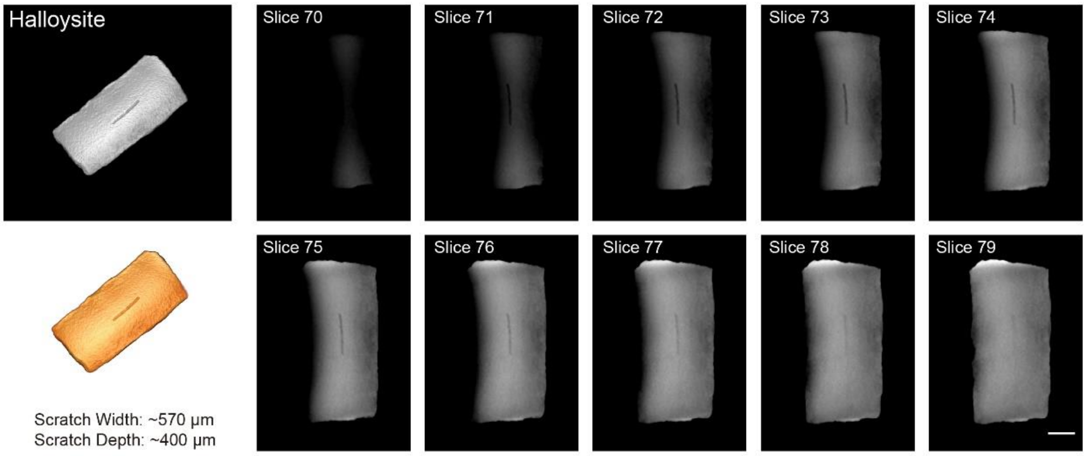

Supplementary Fig. 18 | X-ray microtomography (Micro-CT) experiments show the mechanically-sintered path on a soil-inspired material. Scale bar, 3 mm.

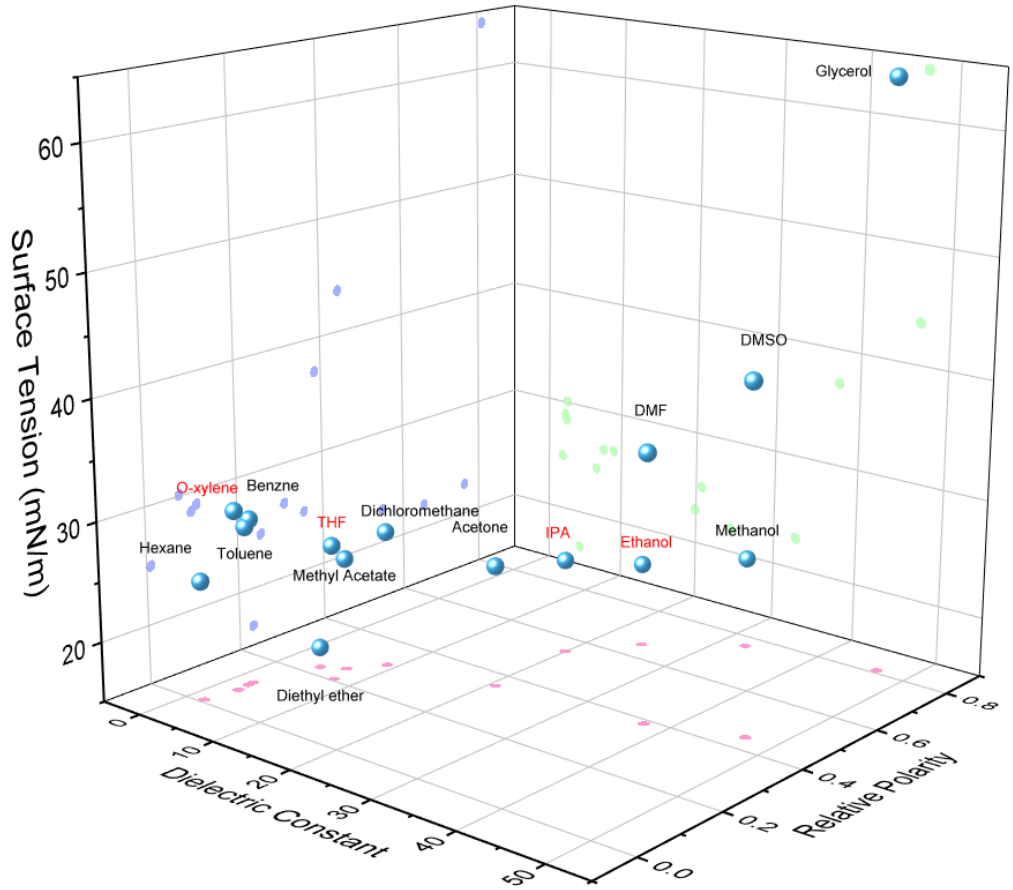

Supplementary Fig. 19 | A 3D plot of the relative polarity, dipole moment, and dielectric constant of tested solvents. Solvents that can erase conductivity are marked with red. Several factors may contribute to erasure of conductivity, including the polarity and dielectric properties of the solvent and their wettability changes on liquid metal at the interface with nanoclay and starch matrix. It is difficult to find universal features of the "working solvents" due to the complexity of the multi-component system.

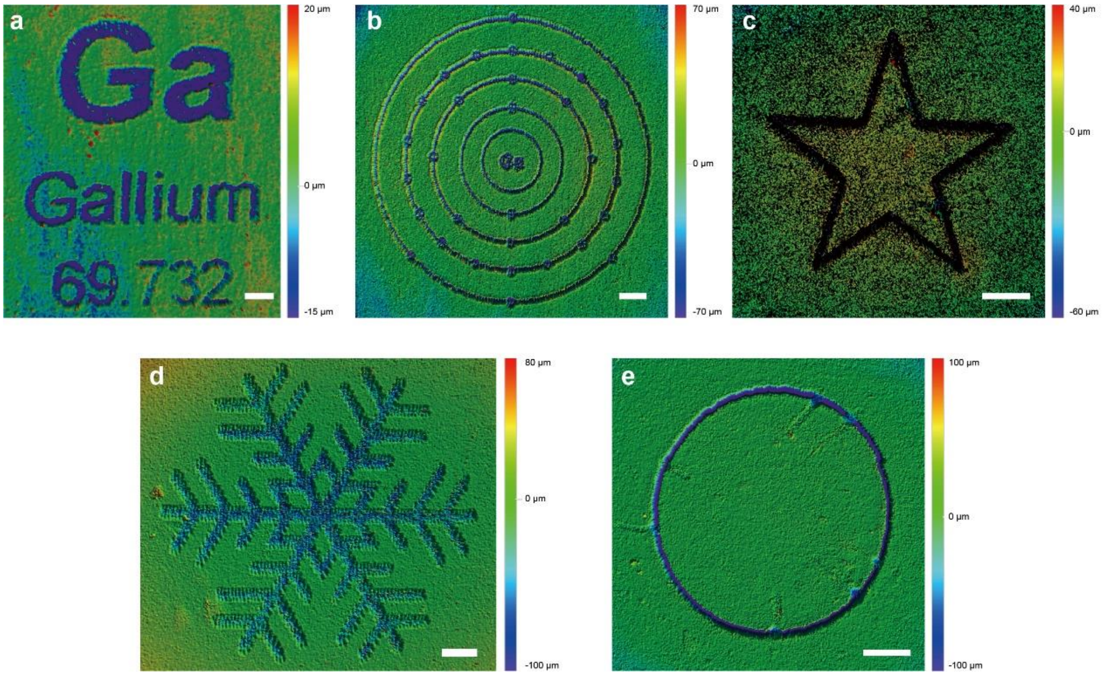

Supplementary Fig. 20 | We can laser-sinter different conductive patterns on the soil-inspired material. The images are taken on a 3D laser confocal scanning microscope, with patterns showing a) the Gallium (Ga) element, b) the electron shell model of Ga, c) a star, d) a snowflake, and e) a circle. Scale bar, 1 mm.

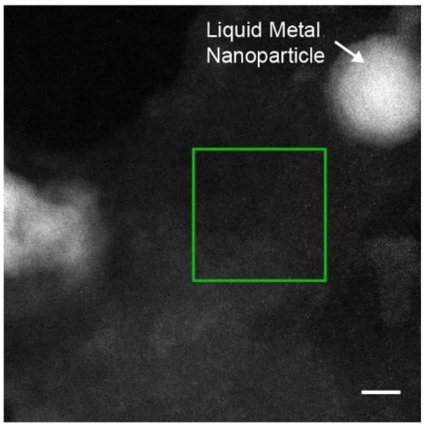

Supplementary Fig. 21 | A scanning transmission electron microscopy (STEM) image of the laser-sintered soil-inspired material. The image shows nanoclay-dominated areas (less electron-dense) with liquid metal nanoparticles (bright sphere, upper right). The area highlighted with a green box contains multiple single atoms. Scale bar, 5 nm.

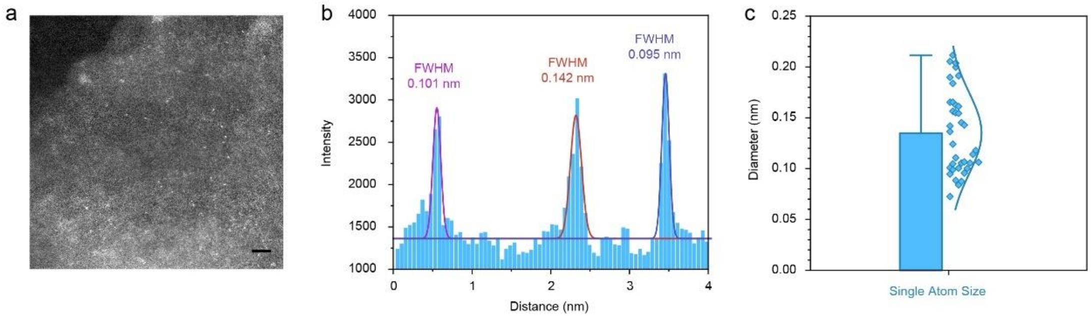

Supplementary Fig. 22 | Gaussian fitting of a line histogram reveals the single atom size. a) A STEM image of a representative area with multiple single atoms on a matrix. Scale bar, 2 nm. b) A typical line histogram with Gaussian fitting calculates the full width at half maximum (FWHM) as the atom size. c) Statistical analysis of single atom sizes shows an average size of ~0.13 nm. Data are presented as mean values ± standard deviation, n = 37.

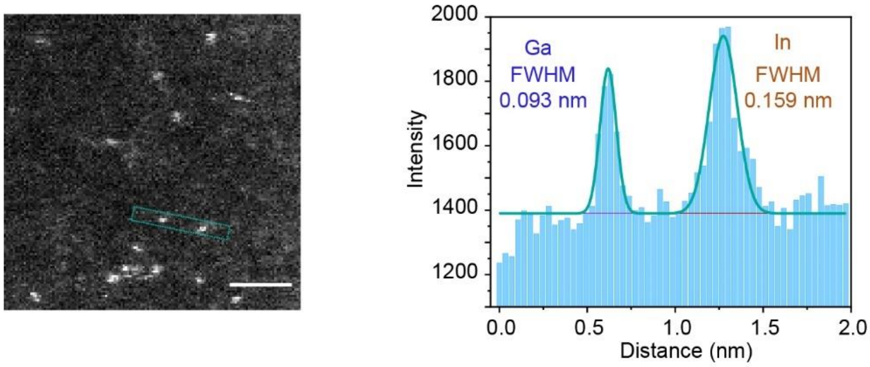

Supplementary Fig. 23 | Electron microscopy (EM) image analysis indicates there are two types of single metal atoms. Several individual atoms can be seen in the STEM image. A line histogram fitted with a Gaussian distribution is used to estimate high-angle annular dark-field (HAADF) imaging intensity and single atom size. With higher signal intensity, the larger atom on the right indicates a higher atomic number, which indicates it is an In atom, while the smaller atom is Ga. Scale bar, 1 nm.

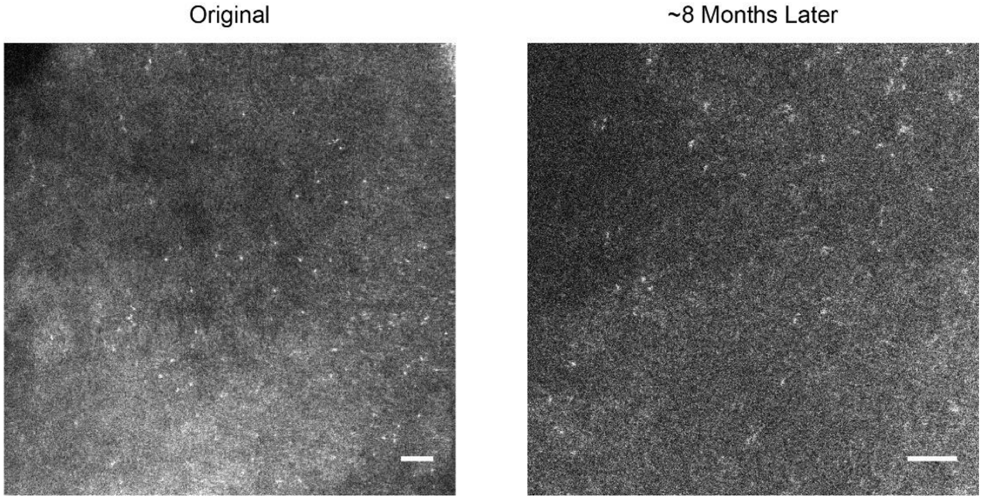

Supplementary Fig. 24 | The single atoms remain stable for at least 8 months after laser sintering. The images were taken on the same sample. Scale bar, 2 nm.

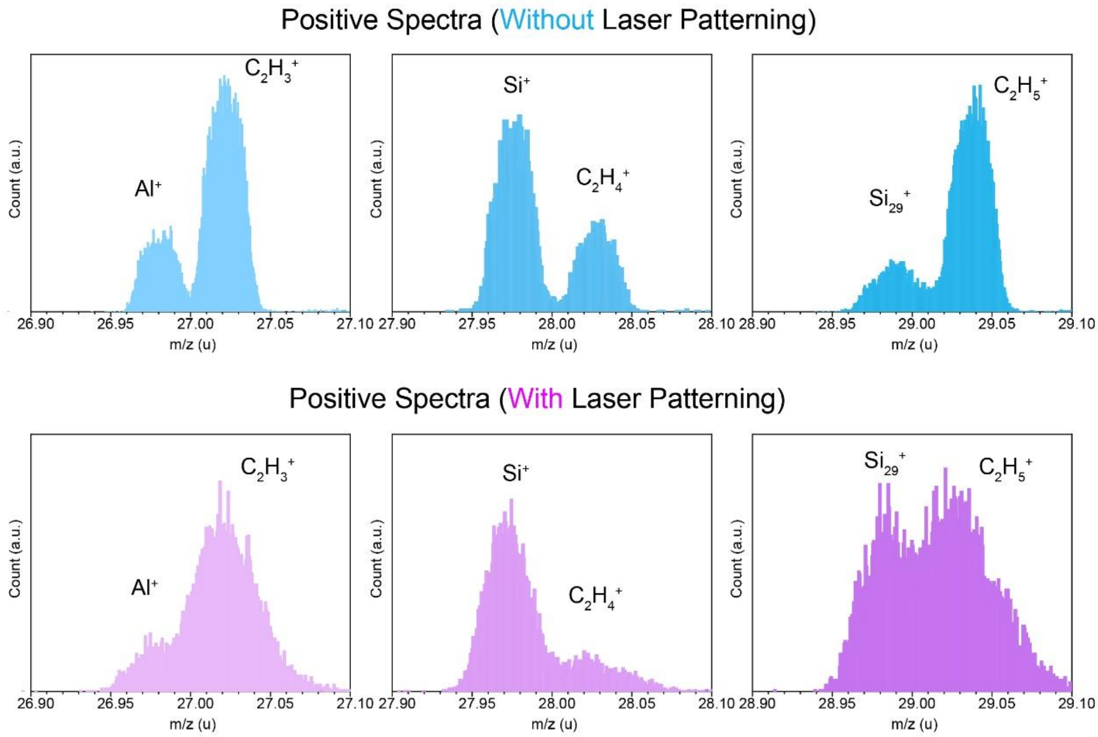

Supplementary Fig. 25 | High-resolution time-of-flight secondary ion mass spectrometry (TOF-SIMS) confirms the existence of Al and Si elements even after laser patterning.

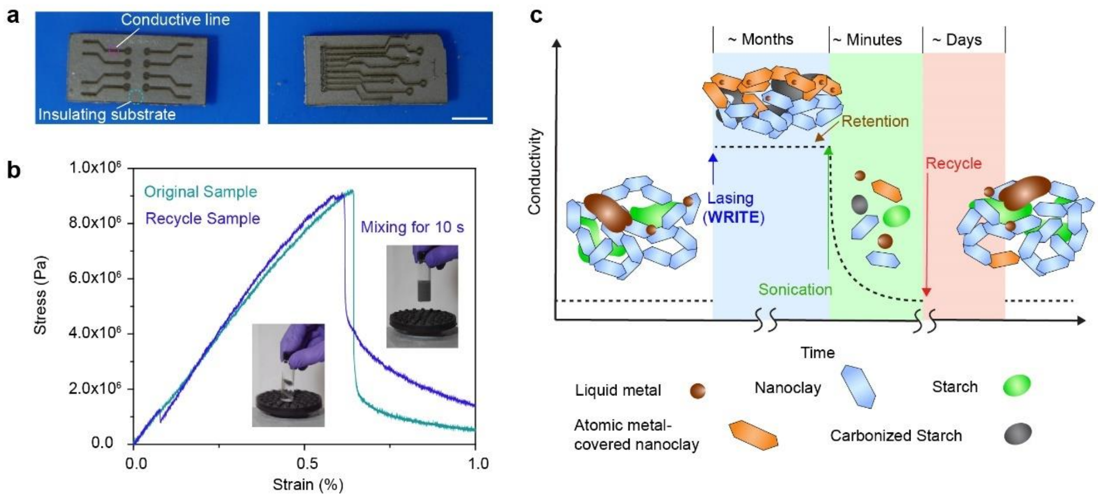

Supplementary Fig. 26 | The soil-inspired material has the potential for recyclable electronics. a) Photographs of two circuit lines made by laser patterning from soil-inspired materials. Scale bar, 5 mm. b) After recycling, soil-inspired material performs almost as well as the original material in terms of mechanical performance. c) Diagram showing how soil-inspired materials can be laser patterned to endow conductivity and then refabricated from recycled materials.

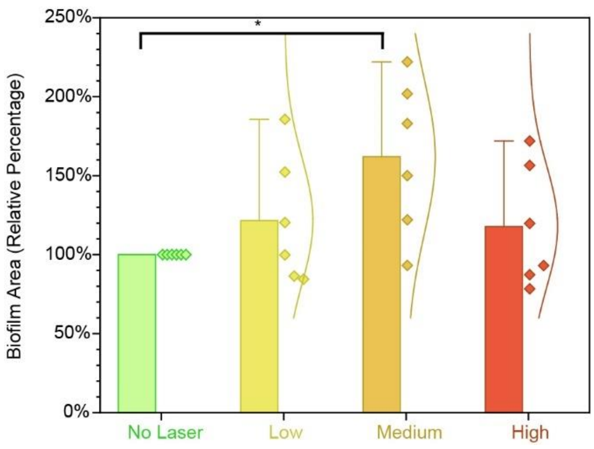

Supplementary Fig. 27 | Suitable laser power can enhance *Bacillus Subtilis* biofilm growth. 'Low', 'Medium', and 'High' labels correspond to 2%, 5%, and 10% laser power, respectively. p = 0.02716, Two-tailed Student's t-test. Data are presented as mean values ± standard deviation (n = 6 for all samples).

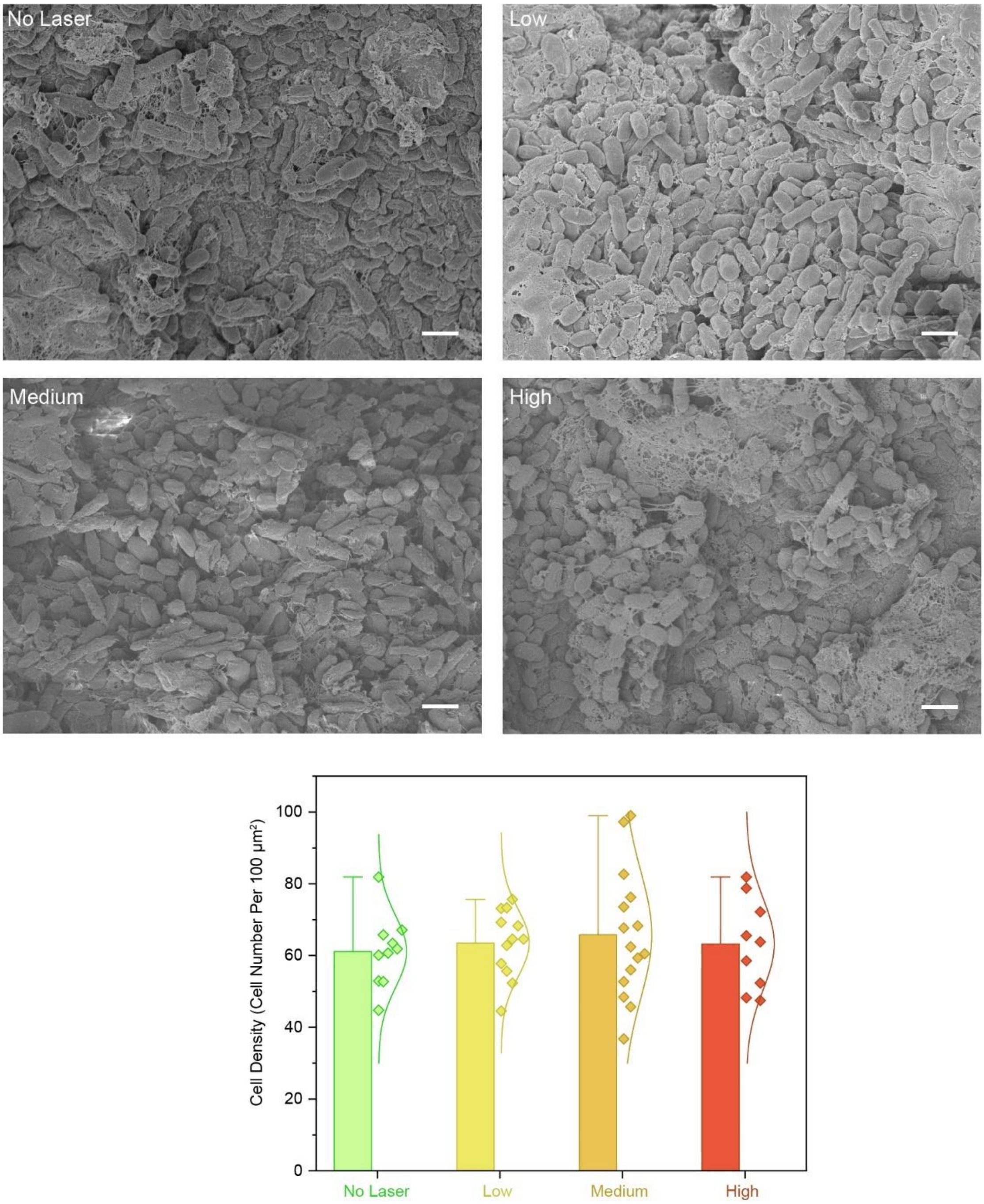

Supplementary Fig. 28 | Biofilm cell density on soil-inspired material is not significantly affected by different laser powers. Scale bars in the SEM images, 2 μm. **'**Low', 'Medium', and 'High' labels correspond to 2%, 5%, and 10% laser power, respectively. Data are presented as mean values ± standard deviation (n = 10, 12, 15, and 10, respectively).

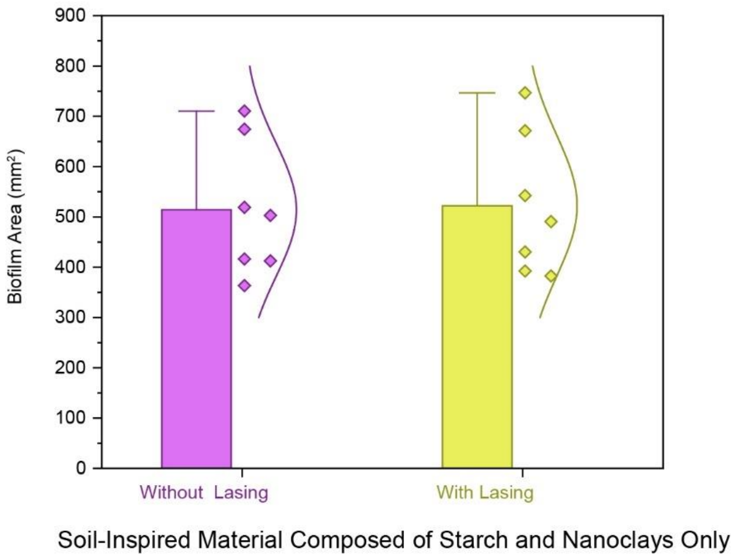

Supplementary Fig. 29 | The benchmark experiment shows that lasing on soil-inspired material without liquid metal does not enhance bacterial growth. Biofilm modulation requires liquid metal, as demonstrated in this experiment. Data are presented as mean values ± standard deviation (n = 7 for both samples).

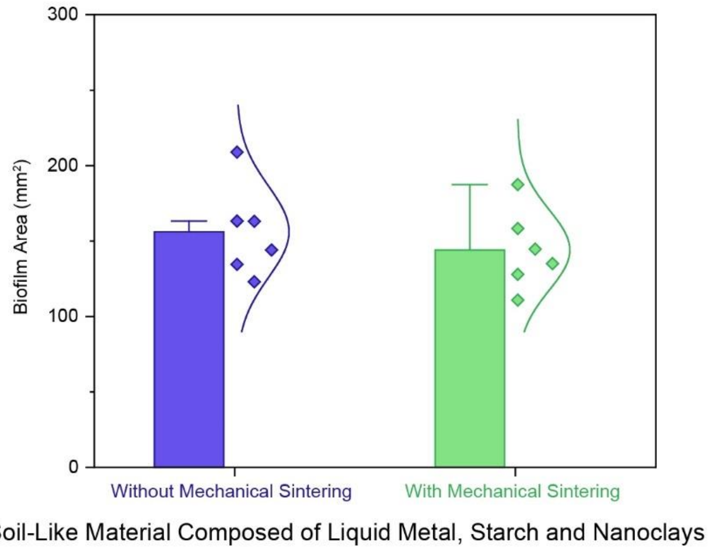

Supplementary Fig. 30 | A benchmark experiment shows that mechanically sintering soil-inspired materials doesn't enhance bacterial growth. It appears that laser sintering, rather than conductivity, is essential to modulating biofilms. Data are presented as mean values ± standard deviation (n = 6 for both samples).

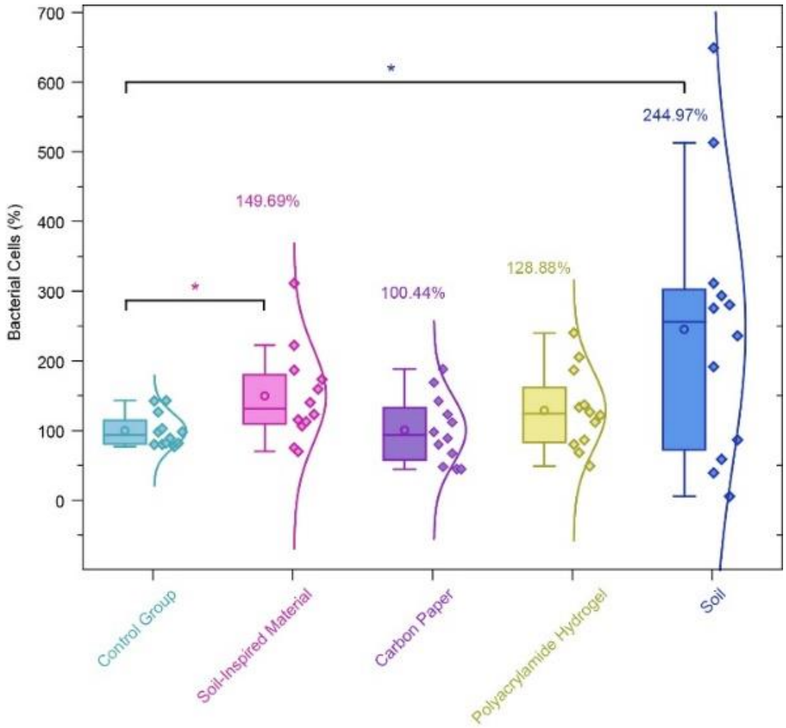

Supplementary Fig. 31 | Liquid flask culture of *Bacillus Subtilis* can be enhanced by soil-inspired materials and soil. The soil-inspired material increases the bacterial cell number to 149.69% ($p = 0.0256$) and soil increases the bacterial cell number to 244.97% ($p = 0.0166$) of control numbers. Two-tailed Student's t-test. Box bind interquartile range (IQR) divided by the median; whiskers extend 1.5 ± IQR ($n = 12$).

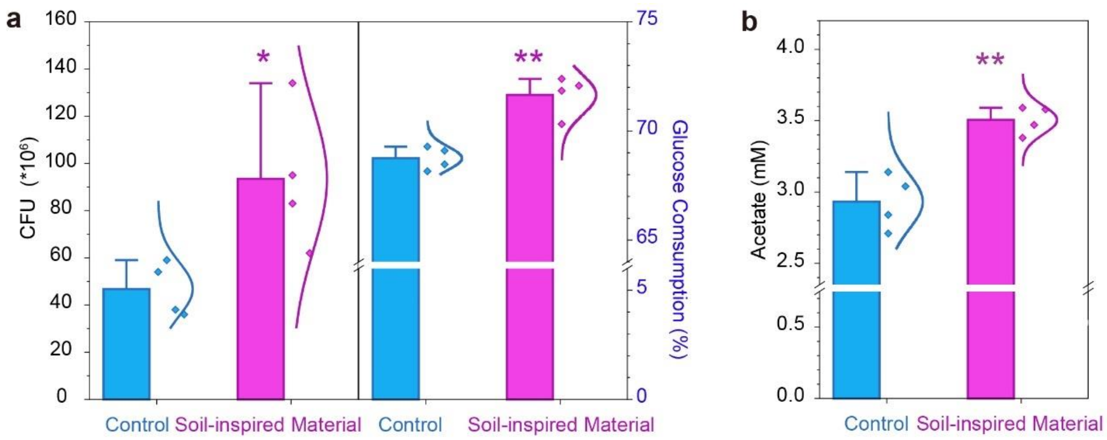

Supplementary Fig. 32 | The soil-inspired material can enhance the growth of *E.coli* in flask culture and enhance biofuel production. a) Soil-inspired material modulates *E. coli* growth in liquid culture, as shown by an increase in colony-forming units (CFU) (p = 0.0278), and improves glucose consumption, the primary carbon source (p = 0.0016). Two-tailed Student's t-test. Data are presented as mean values ± standard deviation (n = 4 for both samples). b) Soil-inspired material modulates bacterial metabolism to produce higher levels of acetate (p = 0.001909). Two-tailed Student's t-test. Data are presented as mean values ± standard deviation (n = 4 for both samples).

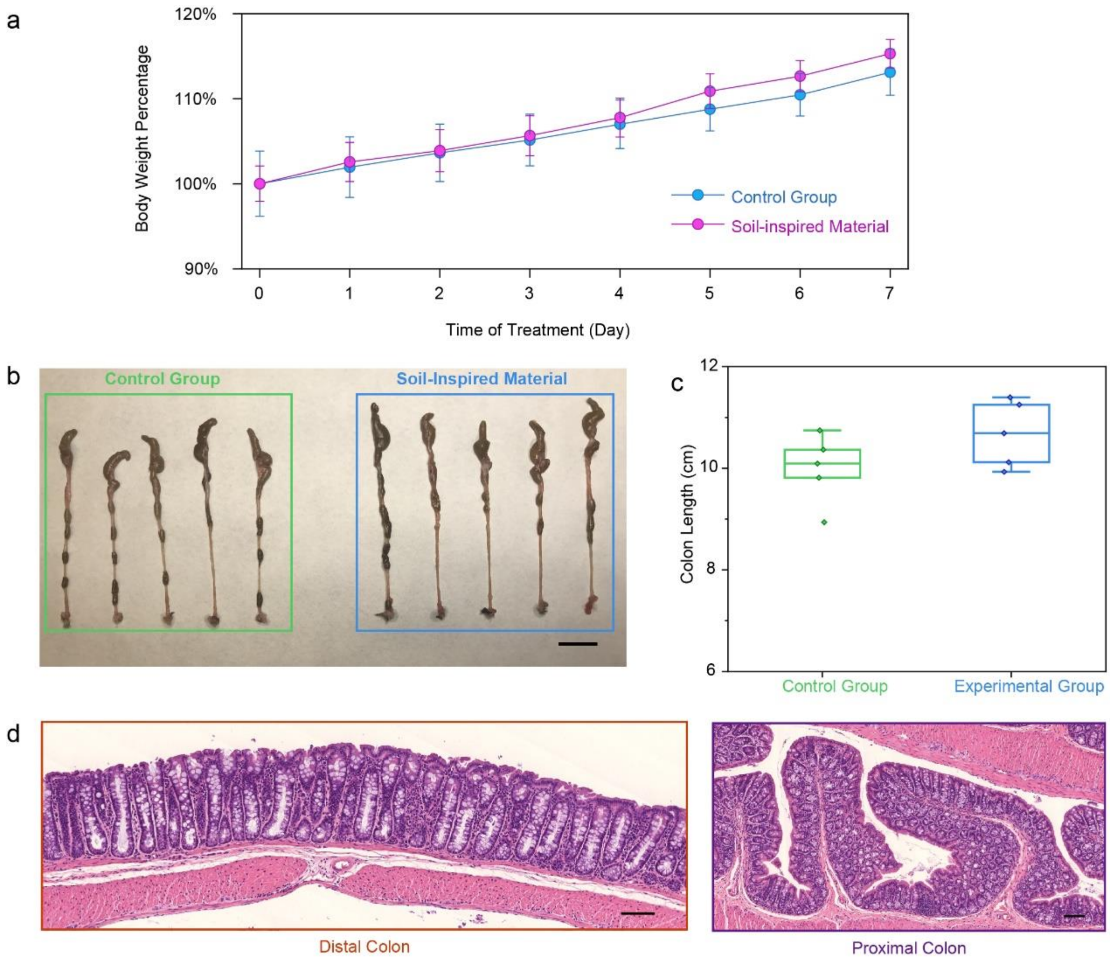

Supplementary Fig. 33 | The soil-inspired material shows good *in vivo* biocompatibility and biosafety. a) The change of mouse body weight percentage over 7 consecutive days with oral administration of soil-inspired material. Results show no difference between treated mice and the control group who received orally administered distilled water, demonstrating the biosafety and biocompatibility of the soil-inspired material. Data are presented as mean values ± standard deviation. b) Optical images of colons from soil-inspired material-treated group and control group. Scale bar, 2 cm. c) Colon length is an important indicator for colon health and is typically shortened with damage or lesions. Statistical analysis shows no difference in colon lengths between the soil-inspired material and control groups. Box bind interquartile range (IQR) divided by the median; whiskers extend 1.5 ± IQR (n = 5). d) Hematoxylin and eosin (H&E) staining of the distal colon and proximal colon from the soil-inspired material group shows a healthy colonic structure. Scale bar, 100 μm.

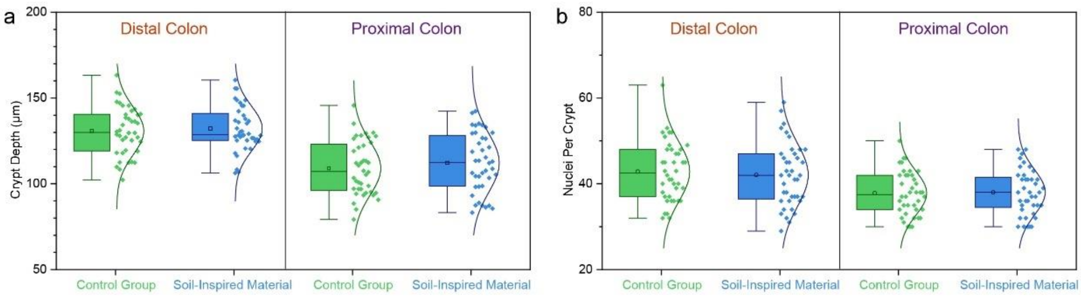

Supplementary Fig. 34 | Quantitative analysis of colon histology confirms a healthy colon following oral administration of soil-inspired material. a) Statistical analysis of the distal and proximal colon crypt depth shows no difference between the soil-inspired material and control groups. Box bind interquartile range (IQR) divided by the median; whiskers extend 1.5 ± IQR (n = 40). b) Statistical analysis of the nuclei per crypt in the distal and proximal colon shows no difference between the soil-inspired material and control groups. Box bind interquartile range (IQR) divided by the median; whiskers extend 1.5 ± IQR (n = 40).

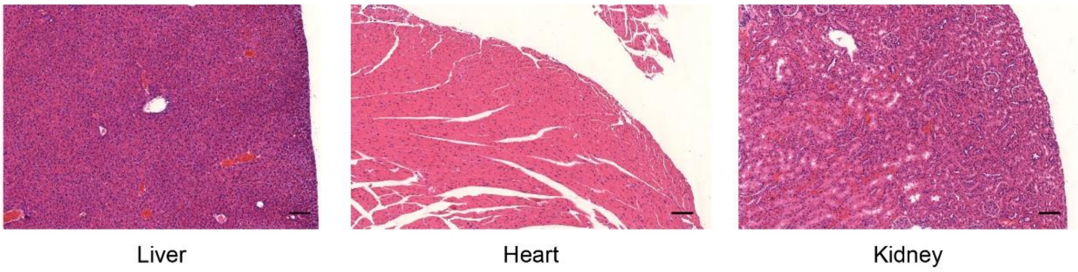

Supplementary Fig. 35 | H&E staining of internal organs confirms the biosafety and biocompatibility of the soil-inspired material. Histology of liver, heart, and kidney shows no lesion or damage, indicating the healthy condition of mice orally administrated with soil-inspired material. Scale bar, 100 μm.

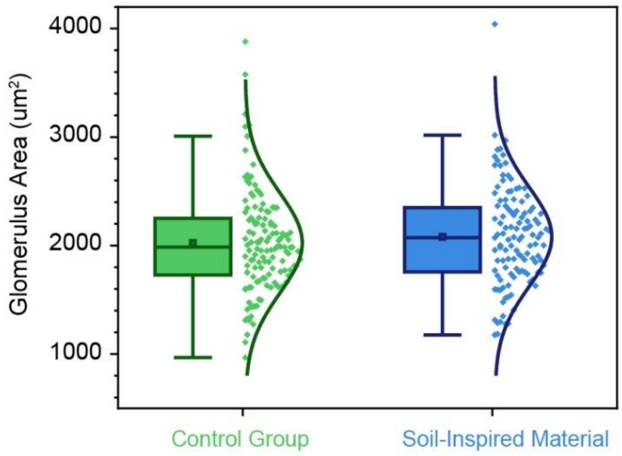

Supplementary Fig. 36 | Quantitative analysis of kidney histology confirms a healthy kidney following oral administration of soil-inspired material. With the nephron as the functional unit, the kidney is responsible for the excretion of waste and harmful chemicals. Statistical analysis of the glomerulus areas within the kidney shows no difference between the soil-inspired material and control groups. Box bind interquartile range (IQR) divided by the median; whiskers extend 1.5 ± IQR (n = 40).

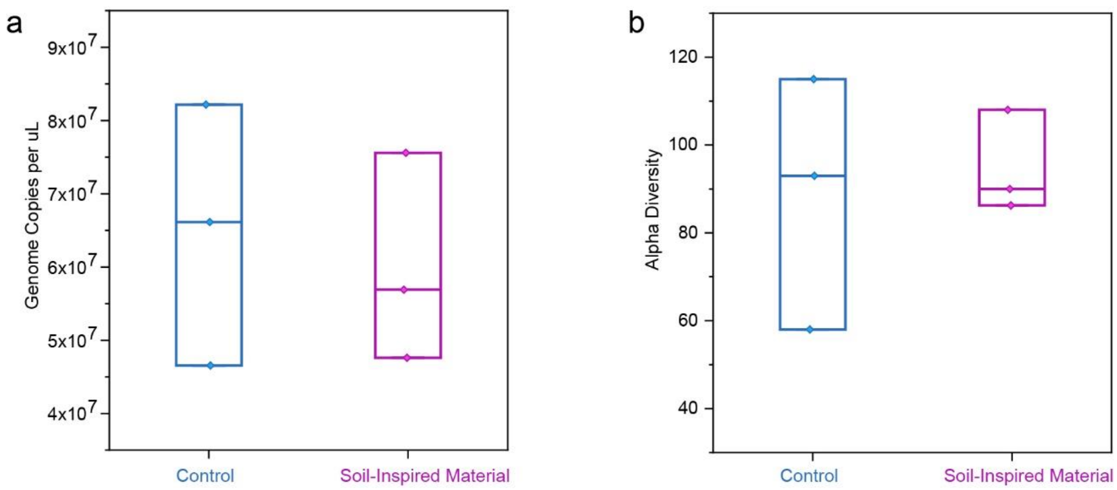

Supplementary Fig. 37 | 16S rRNA Sequencing shows the soil-inspired material does not cause dysbiosis in gut bacteria. a) Statistical analysis on the absolute gene abundance shows no difference between the control and soil-inspired material groups. Box bind interquartile range (IQR) divided by the median; whiskers extend 1.5 ± IQR (n = 3). b) Statistical analysis on the alpha diversity shows no difference between the control and soil-inspired material groups. Box bind interquartile range (IQR) divided by the median; whiskers extend 1.5 ± IQR (n = 3).

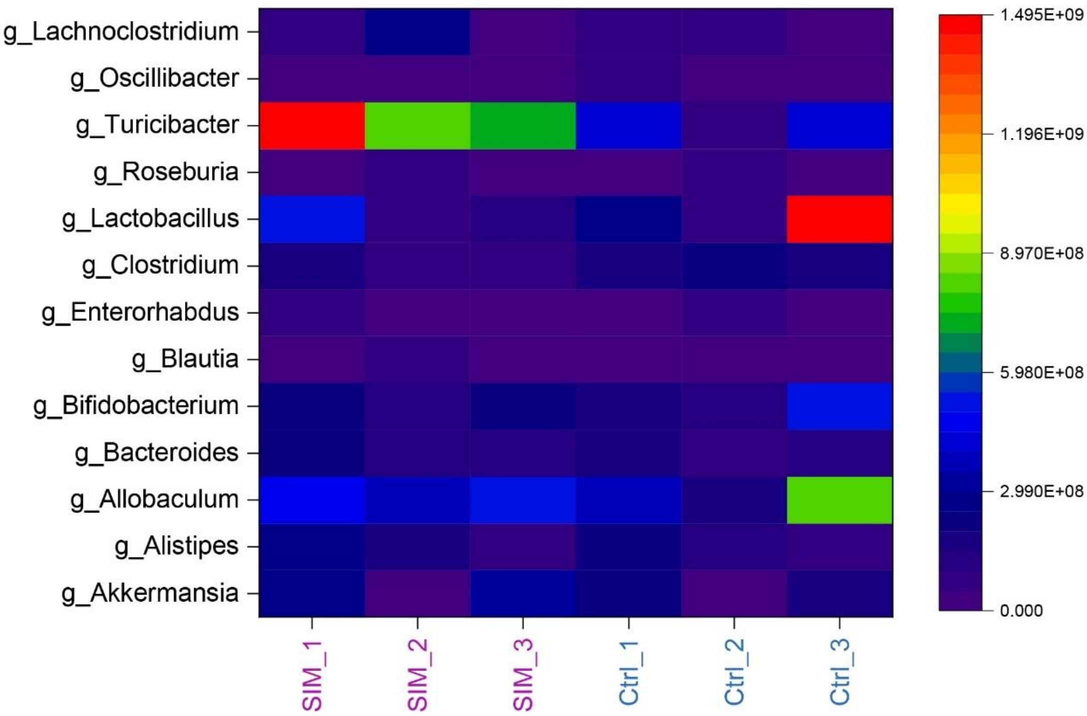

Supplementary Fig. 38 | Taxonomy abundance heatmap indicates no gut microbiota dysbiosis. The absolute abundance of 13 richest genera in gut bacteria, including *g_Akkermansia*, *g_Alistipes*, *g_Allobaculum*, *g_Bacteroides*, *g_Blautia*, *g_Bifidobacterium*, *g_Clostridium*, *g_Enterorhabdus*, *g_Lachnoclostridium*, *g_Lactobacillus*, *g_Roseburia*, *g_Turicibacter*, and *g_Oscillibacter*, was analyzed and plotted as a taxonomy abundance heatmap. There are no statistical differences, indicating no gut microbiota dysbiosis. 'SIM' denotes soil-inspired material.

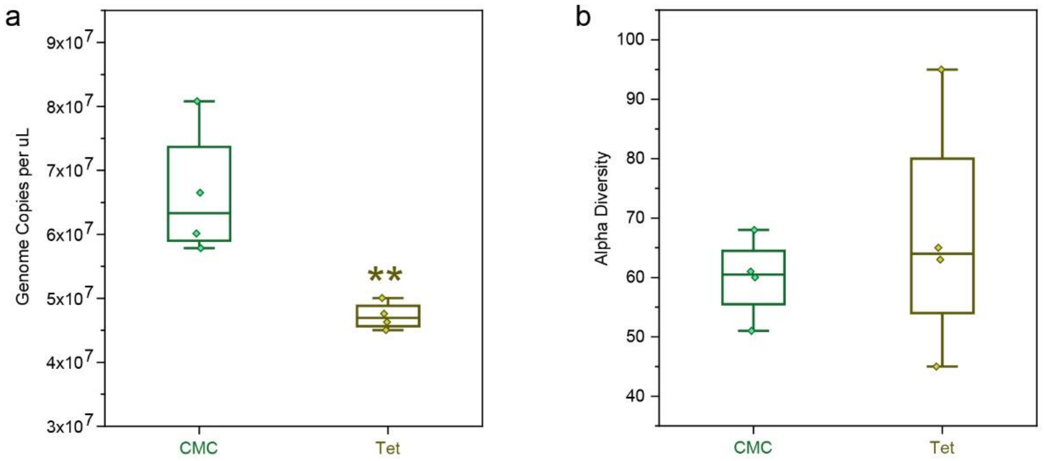

Supplementary Fig. 39 | 16S rRNA Sequencing confirms successful induction of dysbiosis with tetracycline. a) Statistical analysis on the absolute gene abundance shows a significant decrease after tetracycline treatment, indicating dysbiosis in gut bacteria. ($p = 0.011$) Two-tailed Student's t-test. Box bind interquartile range (IQR) divided by the median; whiskers extend 1.5 ± IQR ($n = 4$). b) Statistical analysis on the alpha diversity shows no difference after tetracycline treatment. Box bind interquartile range (IQR) divided by the median; whiskers extend 1.5 ± IQR ($n = 4$). 'CMC' denotes carboxymethyl cellulose.

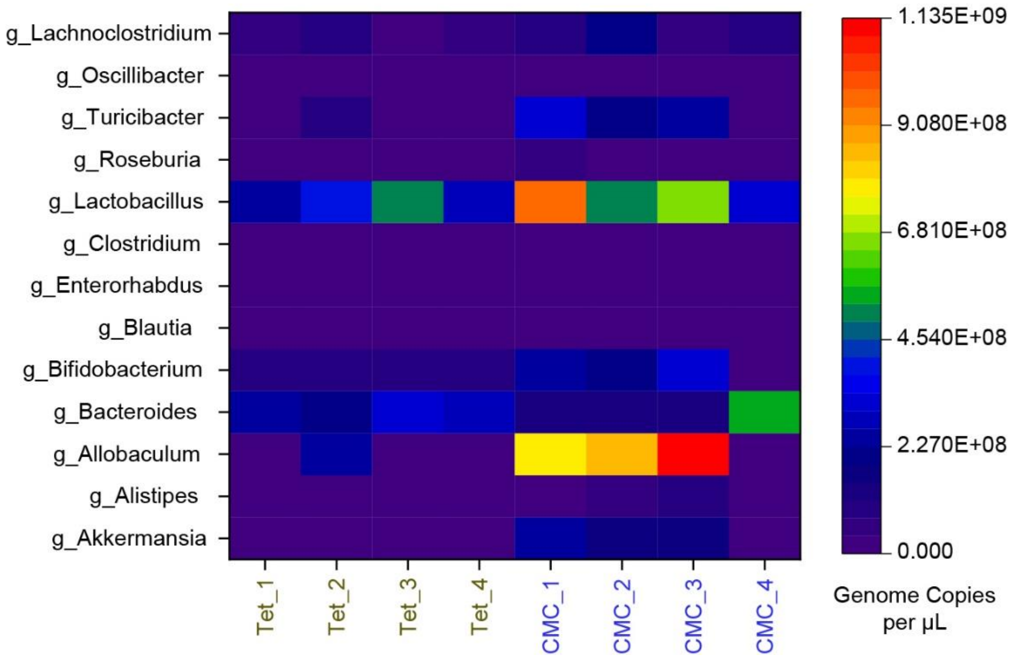

Supplementary Fig. 40 | Taxonomy abundance heatmap of the 13 richest genera confirms tetracycline-induced gut bacteria dysbiosis. The absolute abundance of 5 genera, including *g_Akkermansia*, *g_Alistipes*, *g_Allobaculum*, *g_Clostridium*, and *g_Turicibacter*, was significantly reduced after tetracycline treatment. The vehicle group received an orally administered carboxymethyl cellulose (CMC) suspension.

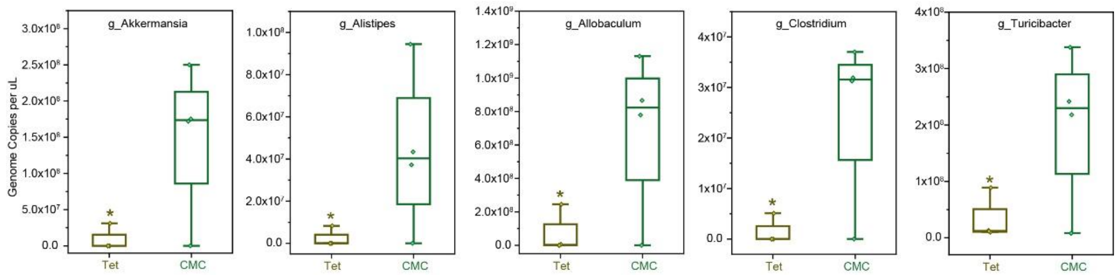

Supplementary Fig. 41 | Tetracycline treatment induces a significant reduction in the absolute abundance of several genera. Five genera, including *g_Akkermansia* (p = 0.019), *g_Alistipes* (p = 0.038), *g_Allobaculum* (p = 0.023), *g_Clostridium* (p = 0.0159), and *g_Turicibacter* (p = 0.02793), were significantly reduced after tetracycline treatment. Two-tailed Student's t-test. Box bind interquartile range (IQR) divided by the median; whiskers extend 1.5 ± IQR (n = 4).

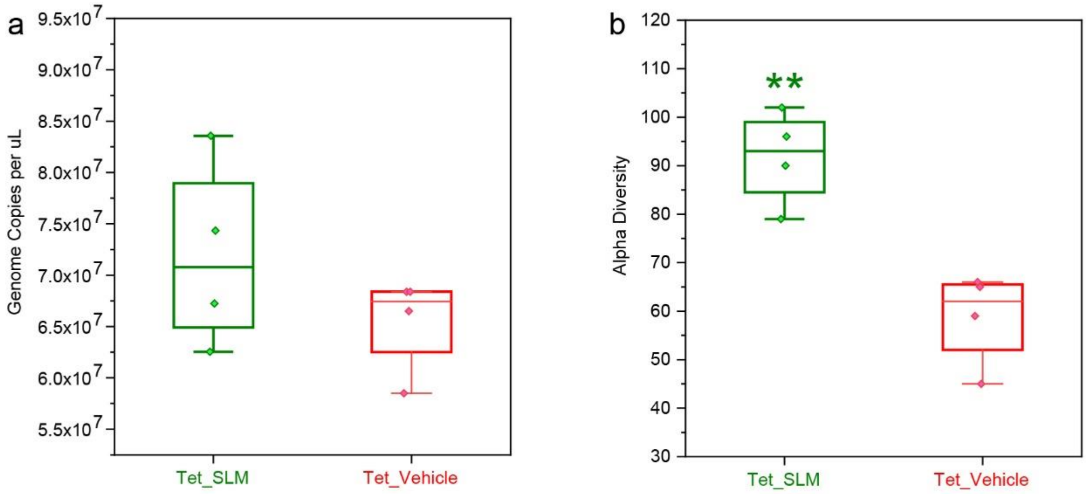

Supplementary Fig. 42 | 16S rRNA Sequencing confirms that soil-inspired material can enrich gut bacteria diversity under pathological conditions. a) Statistical analysis on the absolute gene abundance shows an increase in absolute abundance of the gut bacteria, although not a significant difference. Box bind interquartile range (IQR) divided by the median; whiskers extend 1.5 ± IQR (n = 4). b) Statistical analysis shows treatment with soil-inspired material can significantly increase the alpha diversity, which indicates a healthy microbiota. 'SIM' denotes soil-inspired material (p = 0.003). Two-tailed Student's t-test. Box bind interquartile range (IQR) divided by the median; whiskers extend 1.5 ± IQR (n = 4).

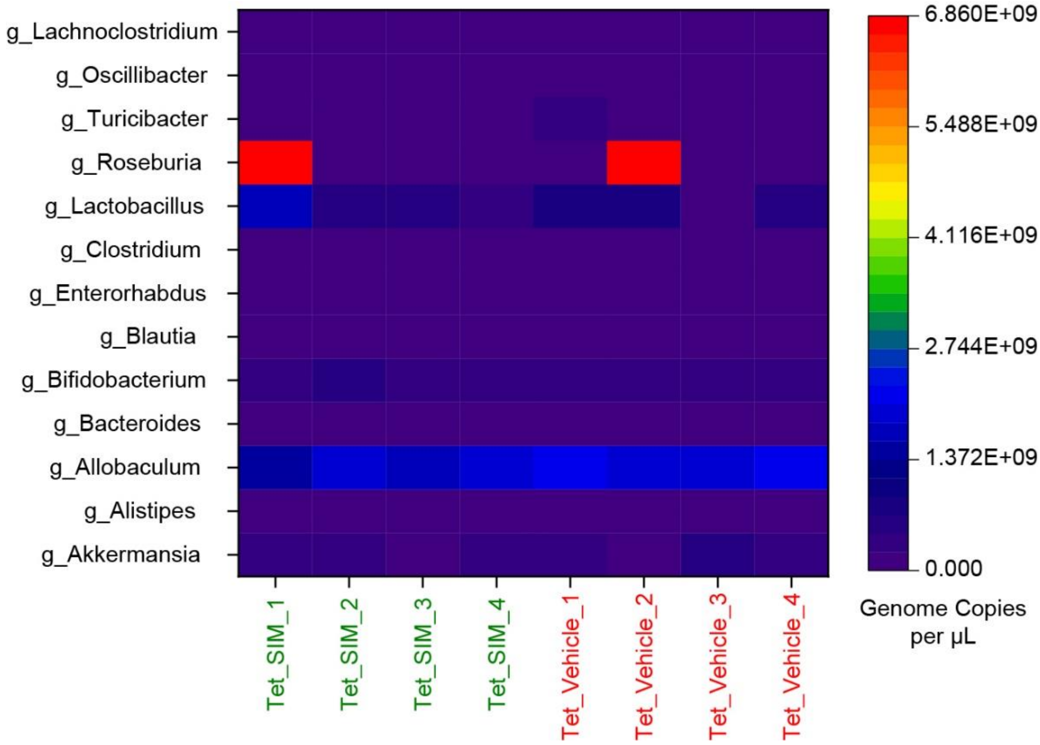

Supplementary Fig. 43 | Soil-inspired material enriches bacterial diversity after gut microbiome dysbiosis induced by tetracycline. Taxonomy abundance heatmap of 13 richest genera shows that the soil-inspired material modulates gut bacteria, with a statistical difference in 4 genera, including *g_Allobaculum*, *g_Oscillibacter*, *g_Blautia*, and *g_Enterorhabdu*.

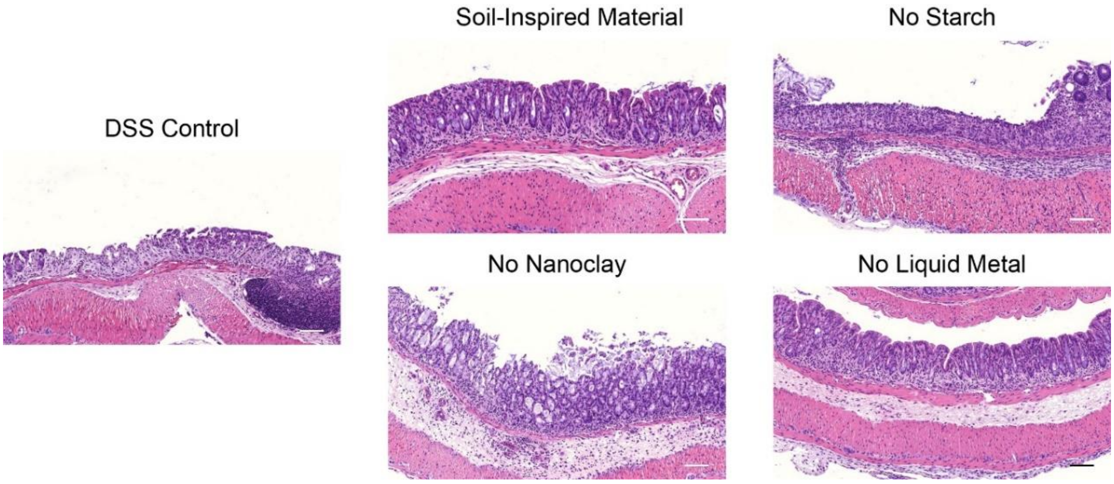

Supplementary Fig. 44 | Representative histology images of the colon region show that the administration of the soil-inspired materials achieved the best protective effect on colonic epithelial intactness, crypt damage, and inflammatory injury in DSS-induced colitis. Scale bar 100 μm.

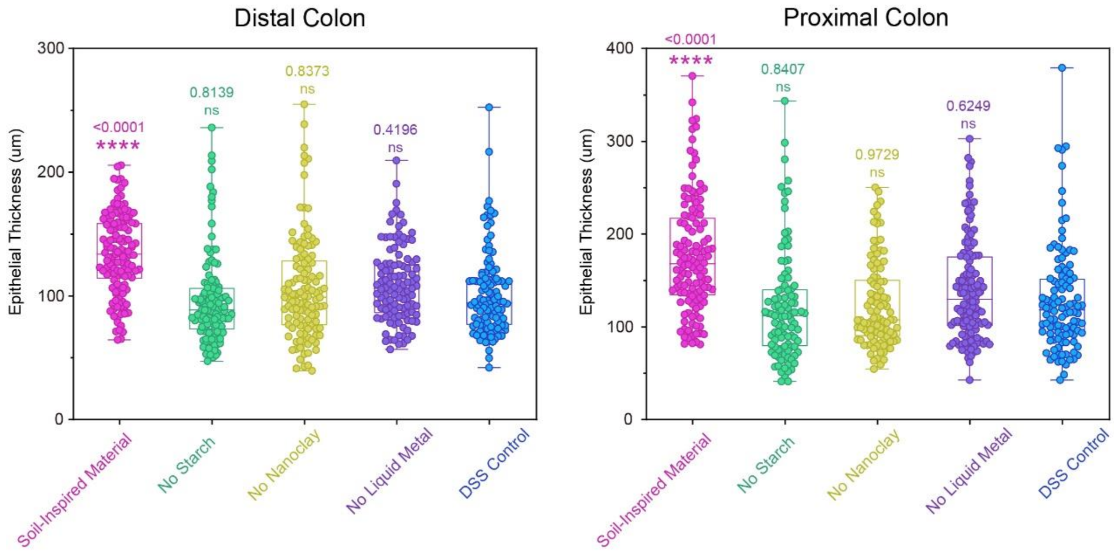

Supplementary Fig. 45 | The soil-inspired material helped maintain the mucus layer (epithelial thickness) in both distal colon and proximal colon in DSS-induced rodent colitis. Boxes bind interquartile range (IQR) divided by the median; whiskers extend 1.5 ± IQR. All datapoints are plotted (n > 100). P values are determined by ordinary one-way ANOVA with Tukey's multiple comparisons test; P value is < 0.0001 (****) for ANOVA summary in both distal colon data and proximal colon data; all the Tukey's multiple comparison shown in figure are between DSS control and corresponding experimental groups. ns, not significant or p > 0.05. Box bind interquartile range (IQR) divided by the median; whiskers extend 1.5 ± IQR (n = 137, 124, 116, 111, 115, 126,101, 101, 135, and 108, respectively).

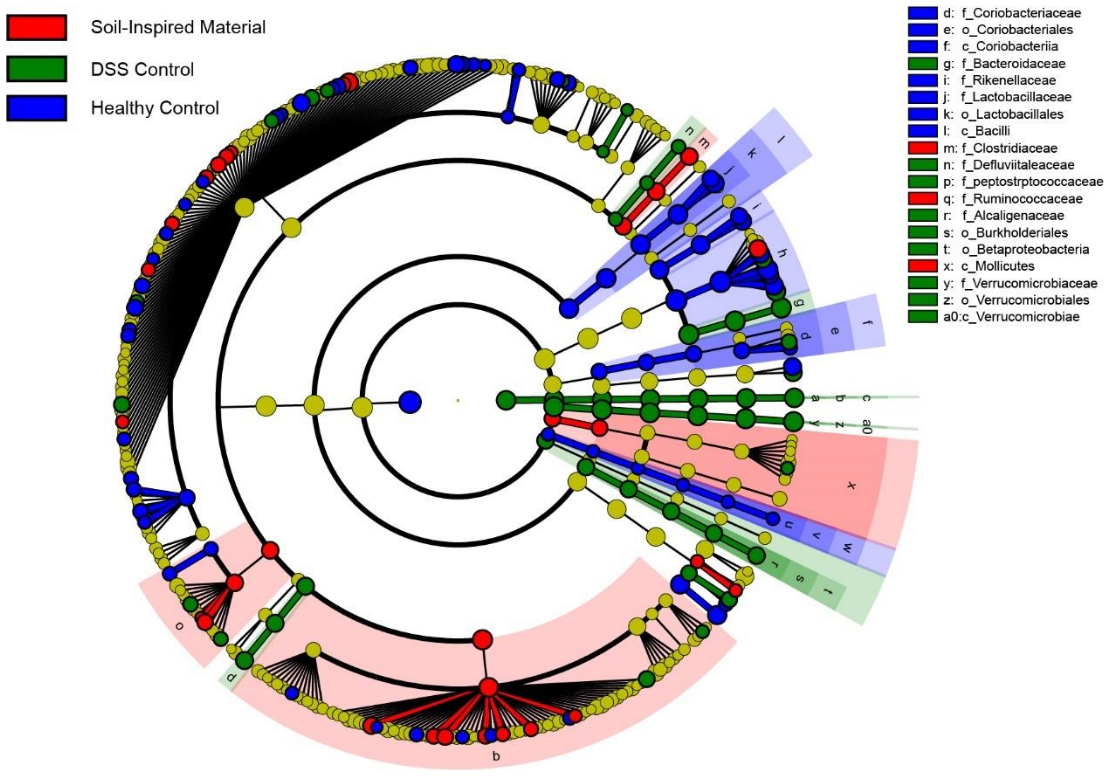

Supplementary Fig. 46 | Linear discriminant analysis Effect Size (LEfSe) taxa analysis confirms that the soil-inspired material alters the microbiome composition compared to healthy and DSS control. The military yellow color indicates the species with no significant difference between groups.

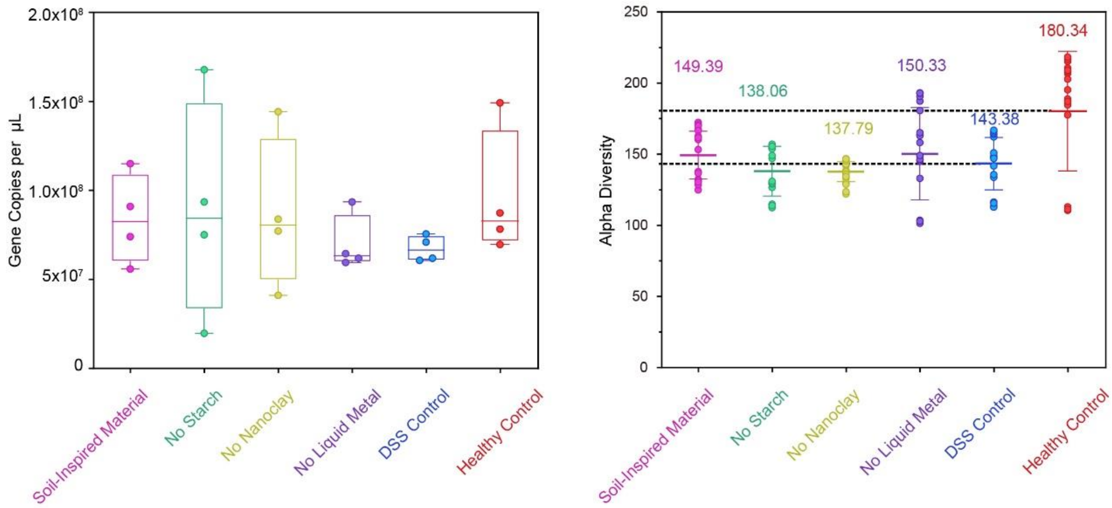

Supplementary Fig. 47 | No significant difference was observed in either absolute gene abundance or alpha diversity of the total fecal bacterium population between experimental groups, including soil-inspired material, no starch, no nanoclay, no liquid metal, DSS treated group, and the healthy control group. P values are determined by ordinary one-way ANOVA with Tukey's multiple comparisons test. n = 4 for absolute gene abundance and n = 40 for alpha diversity. Box bind interquartile range (IQR) divided by the median; whiskers extend 1.5 ± IQR.

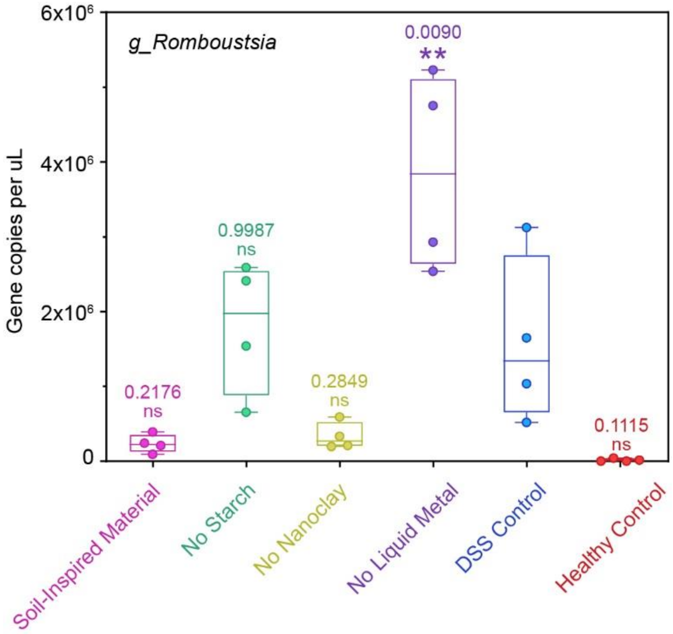

Supplementary Fig. 48 | The material combination without liquid metal (indicated as "No Liquid Metal") significantly worsened the *Romboustsia* dysbiosis induced by DSS treatment, which indicates the potentially positive effect of liquid metal on *Romboustsia* dysbiosis. Boxes bind interquartile range (IQR) divided by the median; whiskers extend 1.5 ± IQR. All datapoints are plotted (n = 4). P values are determined by ordinary one-way ANOVA with Tukey's multiple comparisons test; P value is < 0.0001 (****) for ANOVA summary in both distal colon data and proximal colon data; all the Tukey's multiple comparison shown in figure are between DSS control and corresponding experimental groups. ns, not significant or p > 0.05.

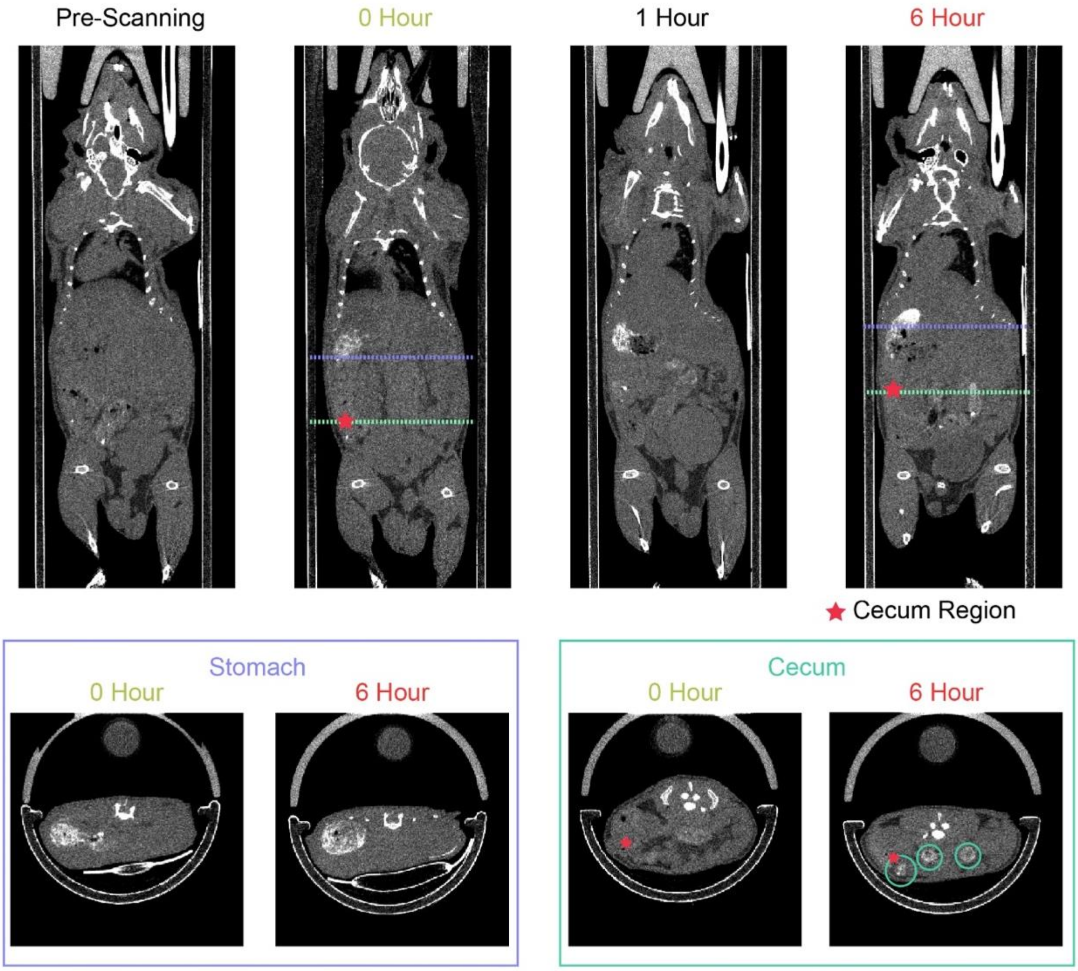

Supplementary Fig. 49 | Micro CT imaging sequence indicates the location of orally administrated soil-inspired material in gastrointestinal tracts.

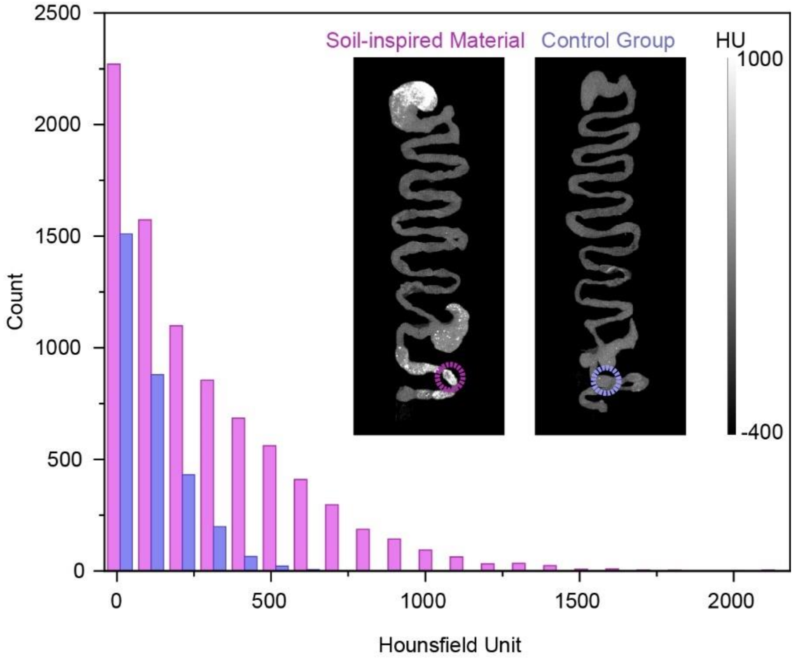

Supplementary Fig. 50 | *Ex-vivo* comparison of gastrointestinal tract 6 hours following oral administration of soil-inspired material and control gastrointestinal tissue without exposure to the material. The CT images indicate the distribution of soil-inspired material in the colon region and the accumulation in feces (highlighted with circles). The histogram presents the numbers of pixels of the highlighted circles in the images in terms of their radio intensity (in the Hounsfield unit).

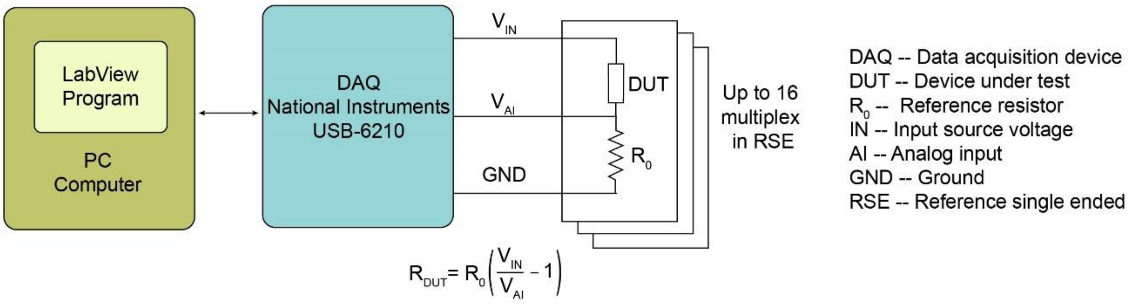

Supplementary Fig. 51 | System developed for real-time conductivity measurement with multiple samples under solvent exposure.

Supplementary Videos

Supplementary Video 1: Focused ion beam scanning electron microscopy (FIB-SEM) images of a soil-inspired material show the porosity, which is consistent with x-ray ptychography and fluorescence imaging, and cross-sectional TEM images.